

Figuring Out Gas & Galaxies In Enzo (FOGGIE). XIV. The Observability of Emission from Accretion and Feedback in the Circumgalactic Medium with Current and Future Instruments

VIDA SAEEDZADEH ¹, JASON TUMLINSON ^{2,1}, MOLLY S. PEEPLES ^{2,1}, BRIAN W. O'SHEA ^{3,4,5,6},
CASSANDRA LOCHHAAS ^{7,8}, LAUREN CORLIES ⁹, CAMERON W. TRAPP ¹, BRITTON D. SMITH ¹⁰,
JESSICA K. WERK ¹¹, AYAN ACHARYYA ¹², RAMONA AUGUSTIN ¹³, ANDREW J. FOX ², NICOLAS LEHNER ¹⁴ AND
ANNA C. WRIGHT ¹⁵

¹Center for Astrophysical Sciences, William H. Miller III Department of Physics & Astronomy, Johns Hopkins University, 3400 N. Charles Street, Baltimore, MD 21218

²Space Telescope Science Institute, 3700 San Martin Dr., Baltimore, MD 21218

³Department of Computational Mathematics, Science, and Engineering, Michigan State University, East Lansing, MI, US

⁴Department of Physics and Astronomy, Michigan State University, East Lansing, MI, US

⁵Facility for Rare Isotope Beams, Michigan State University, East Lansing, MI 48824, USA

⁶Institute for Cyber-Enabled Research, 567 Wilson Road, Michigan State University, East Lansing, MI 48824

⁷Center for Astrophysics, Harvard & Smithsonian, 60 Garden St., Cambridge, MA 02138

⁸NASA Hubble Fellow

⁹University of California Observatories/Lick Observatory, Mount Hamilton, CA 95140, USA

¹⁰Institute for Astronomy, University of Edinburgh, Royal Observatory, EH9 3HJ, UK

¹¹University of Washington, Department of Astronomy, Seattle, WA 98195, USA

¹²INAF - Astronomical Observatory of Padova, vicolo dell'Osseatorio 5, IT-35122 Padova, Italy

¹³Leibniz-Institut für Astrophysik Potsdam (AIP), An der Sternwarte 16, 14482 Potsdam, Germany

¹⁴Department of Physics, University of Notre Dame, Notre Dame, IN 46556

¹⁵Center for Computational Astrophysics, Flatiron Institute, 162 Fifth Avenue, New York, NY 10010

ABSTRACT

Observing the circumgalactic medium (CGM) in emission lines from ionized gas enables direct mapping of its spatial and kinematic structure, offering new insight into the gas flows that regulate galaxy evolution. Using the high-resolution Figuring Out Gas & Galaxies In Enzo (FOGGIE) simulations, we generate mock emission-line maps for six Milky Way-mass halos. Different ions (e.g., H I, O VI) trace distinct CGM phases and structures, highlighting the importance of observations in multiple species. We quantify the observable CGM mass fraction as a function of instrument spatial resolution and surface brightness sensitivity, finding that sensitivity is the dominant factor limiting detectability across all ions. At fixed sensitivity, higher spatial resolution reveals more structures; at fixed spatial resolution, higher sensitivity recovers a higher percentage of the total mass. We explore CGM kinematics by constructing emissivity-weighted projected velocity maps and comparing line-of-sight velocities between ions. O VI shows the largest kinematic deviation from H I, while Mg II and Si II most closely follow H I velocities. Distinguishing these phases out to 50kpc from the galaxy center requires spectral resolution better than 30km/s for most ion pairs. Additionally, separating inflowing from outflowing gas based on projected kinematics also requires high spectral resolution: at 30km/s, more than 80% of gas above the emission detection threshold can be distinguished kinematically, but this fraction drops to < 40% with a resolution of 200km/s. Our results provide predictions for future UV and optical instruments, showing that recovering the multiphase structure and kinematics of circumgalactic emission will require both high sensitivity and fine kinematic resolution.

Keywords: Galaxies (573) — Circumgalactic medium (1879) — Hydrodynamical simulations (767) — Extragalactic astronomy (506)

1. INTRODUCTION

The circumgalactic medium (CGM) is the region around galaxies through which they acquire gas for star formation, the destination for outflows from supernovae and AGN, and the site of recycling of recent outflows into future accretion (J. Tumlinson et al. 2017; C.-A. Faucher-Giguère & S. P. Oh 2023). Since it was first noticed in the 1960s, the CGM has been studied intensively to understand its role in fueling galactic accretion and star formation. Primarily from absorption-line observations, we have good evidence that the CGM bears a significant fraction of galactic baryons (J. K. Werk et al. 2014) and metals (M. S. Peeples et al. 2014), that the material observed is usually consistent with being bound to the host galaxy (at least at low redshift) (S. Borthakur et al. 2016), that there is a range of metallicities indicating diverse origins in accretion, feedback, and recycling (N. Lehner et al. 2013; J. X. Prochaska et al. 2017), and that quenched galaxies show a distinct behavior with less overall gas and a different range of ionization states (F. S. Zahedy et al. 2019).

Most of the detailed information we have about the CGM comes from absorption-line measurements using distant QSOs (or sometimes stars) as background sources. These techniques date back to the 1960s, shortly after the discovery of QSOs themselves (J. N. Bahcall & L. Spitzer 1969). Most of these absorber observations were obtained without prior knowledge of the foreground galaxy’s redshift, mass, or separation from the sightline. Only in the last 15 years has it become possible, with large-area galaxy surveys and efficient UV/optical spectrographs, to choose a particular set of galaxies and efficiently probe the CGM as a function of mass, redshift and other properties. These observations excel at measuring CGM gas even down to very low mass density by combining sensitive spectroscopy from ground and space-based telescopes.

Yet even state-of-the-art surveys of the CGM using the largest available samples of QSO absorbers (J. Tumlinson et al. 2013; N. M. Nielsen et al. 2013) are limited to tens or hundreds of objects, and in most cases each galaxy collected in a sample is probed by only one background QSO. There are exceptions in the nearby Universe, where galaxies subtending large areas on the sky can be probed by > 10 background objects (e.g.; D. V. Bowen et al. 2016; D. Krishnarao et al. 2022), with up to ~ 50 in the case of the nearby M31 (N. Lehner et al.

2020, 2025a). But generally, the maps of the CGM that we can compare to theoretical models or hydrodynamical simulations are highly averaged - over azimuthal bands in radius, and usually across galaxy mass. Careful attention to galaxy orientation with high-quality imaging has allowed some groups to study the azimuthal dependence of CGM absorption, which shows a preference for the minor axis of disks in a way that suggests galactic winds (G. G. Kacprzak et al. 2012; R. Bordoloi et al. 2014; T.-W. Lan & H. Mo 2018; M. Wendt et al. 2021; A. Shaban et al. 2025). The resulting averages are informative, but they lose the rich 3D structure and dynamic balance that we expect is really there.

To make progress beyond the 1D picture, we must strive to obtain projected 2D distributions of the real 3D CGM. There are several approaches to this. Strong gravitational lensing can provide highly-extended background galaxies that are useful for probing the CGM of foreground galaxies in 2D (e.g., S. Lopez et al. 2020; R. Augustin et al. 2021; R. Bordoloi et al. 2022). However the most promising technique of all is to map the CGM of galaxies with emission from the gas itself, making background sources of all kinds irrelevant and permitting 2D maps of the CGM gas of individual galaxies with much less ambiguity, with spectra providing a third dimension. Recognizing the potential of emission observations to advance our understanding of the baryon cycle through galaxies, the Astro2020 Decadal Survey listed “Mapping the Circumgalactic and Intergalactic Medium in Emission” as one of the key Discovery Areas for this decade.

Many pioneering observations of CGM emission already exist from UV and optical measurements. The first feasible spectroscopic searches for circumgalactic O VI were made with NASA’s Far Ultraviolet Spectroscopic Explorer (FUSE), which launched in 1999. In the first search for emission around external galaxies with FUSE, B. Otte et al. (2003) detected O VI emission above the disk of the edge-on spiral NGC 4631, coinciding with emerging feedback seen in $H\alpha$ imaging. H. Chung et al. (2021a) revisited these FUSE data and reported four O VI detections in NGC 4631 and NGC 891. With archival FUSE data, J.-A. Kim et al. (2024) were able to detect O VI emission in the prototypical M82 galactic superwind. FUSE also detected O VI emission in a local “Lyman break” galaxy Haro 11 (J. P. Grimes et al. 2007). The Solar Blind Channel on the Hubble Advanced Camera for Surveys (ACS/SBC) enables a differential imaging technique for O VI by subtracting two filter bandpasses that cover O VI and the nearby continuum. In their pioneering deployment of this method, M. Hayes et al. (2016) identified O VI emission extended

over ~ 20 kpc surrounding the disk of a star-bursting galaxy. With similar techniques, [J.-A. Kim et al. \(2024\)](#) mapped O VI in the Makani superwind and related it to lower ion emission mapped in the optical with Keck Cosmic Web Imager. [P. Morrissey et al. \(2018\)](#) and [L. Wisotzki et al. \(2018\)](#) used VLT/MUSE to find that nearly every high-redshift galaxy has a Ly α halo.

In addition to these CGM/halo emission line detections with existing instrumentation, there are now operating and planned instruments that are purpose-built and optimized for this faint light. Operational instruments include the FIREBALL-2 balloon payload, last flown in 2023 ([D. M. Miles et al. 2025](#)), the Circumgalactic H α Spectrograph (CHaS, [N. Melso et al. 2024](#)), and the Dragonfly Spectral Line Mapper ([S. Chen et al. 2025](#)). Planned instruments include the Aspera CubeSat that plans to map O VI in a sample of nearby galaxies ([H. Chung et al. 2021b](#)) and the proposed JUNIPER CubeSat ([E. M. Witt et al. 2025](#)) that is optimized for multiple low- and high-ionization UV ions.

In light of increasing prospects for multi-ion maps using UV ions (observed from space, below the UV atmospheric cutoff, or from the ground at significant redshift), we consider the requirements and benefits of observing CGM emission in a key set of UV diagnostic lines. In particular, we analyze a high-resolution set of simulations from the FOGGIE suite ([M. S. Peeples et al. 2019](#); [R. C. Simons et al. 2020](#); [A. C. Wright et al. 2024](#)) to assess the detectability of multiphase gas. This paper builds on the foundation of previous work with FOGGIE to predict CGM emission at $z = 3$ ([L. Corlies et al. 2020](#)) and lower redshifts ([C. Lochhaas et al. 2025](#)); see also similar work by [R. Augustin et al. \(2019\)](#) based on RAMSES simulations and [D. Lokhorst et al. \(2019a\)](#) in the EAGLE simulations. Our primary goal is to assess the observational feasibility of separating galactic inflows and outflows from disk gas, and to assess the instrument performance limits that must be achieved to make this feasible.

In Section 2 we describe our simulations and analysis methods. In Section 3 we describe the multi-ion emission-line results. Section 4 evaluates how much CGM mass can be detected as a function of observational limits. Section 5 investigates how inflows, outflows, and disk can be separated kinematically. Section 6 places these results in the context of specific instruments, current and planned. Section 7 summarizes our conclusions.

2. SIMULATIONS AND METHODS

In this Section, we explain the hydrodynamical simulation used for analysis (Section 2.1), how we defined

and removed the H I disk (Section 2.2) and how the gas emissivity is calculated (Section 2.3).

2.1. Simulations

For the analysis in this paper we use the FOGGIE (Figuring Out Gas & Galaxies In Enzo) simulations. FOGGIE uses the Enzo Adaptive Mesh Refinement (AMR) code ([G. L. Bryan et al. 2014](#); [C. Brummel-Smith et al. 2019](#)) which enables customized placement of high-resolution grids according to an adaptive, multi-criteria refinement scheme. These refinement schemes are designed to optimize the simulations for resolving the circumgalactic medium (CGM) at levels not usually achieved in cosmological simulations. In this study, we analyze all six FOGGIE halos at $z = 0.5$. These halos were originally selected to be Milky Way-mass halos at $z = 0$, and they undergo no major mergers after $z = 2$ (see [A. C. Wright et al. 2024](#))¹⁶. Because the growth of the FOGGIE halo is dominated by minor mergers over most of cosmic time, their total mass evolves slowly, and they already reside in the Milky Way mass range at $z = 0.5$. We base our analysis at $z = 0.5$ because the CGM in FOGGIE is more structured and dynamic at intermediate redshifts than at $z = 0$, where star formation and CGM small-scale structure are less prominent. Selecting halos at $z = 0.5$ ensures a snapshot of a wider range of CGM morphologies is still present, enhancing the diversity of physical conditions probed. We assume that the variety of structures captured at this redshift is representative of those seen in the low-redshift universe.

As described in [M. S. Peeples et al. \(2019\)](#), FOGGIE uses a “forced refinement” technique, in which a comoving cubic region 200 kpc/ h comoving on a side is centered on the galactic center of mass as it moves through the domain. Within this moving box, cells are refined until the maximum cell size in the box is 1100 pc. [L. Corlies et al. \(2020\)](#) found that this refinement scheme improved the sampling of the density, temperature, and metallicity fields of CGM gas, resolving smaller structures and even the internal ionization structures of small clouds. Similar forced-refinement techniques have been used to good effect in other studies that are optimized to resolve the CGM ([F. van de Voort et al. 2019](#); [C. B. Hummels et al. 2019](#)).

Another “cooling refinement” criterion was first introduced in [R. C. Simons et al. \(2020\)](#): within the refinement box, cells are further refined if their cooling time is shorter than their local sound-crossing time. These cells reach sizes as small as 274 pc at $z = 0$ (or 183 pc at $z = 0.5$). This combined refinement approach ensures

¹⁶ One exception: Squall has a 2:1 merger at $z = 0.7$.

Table 1. The halo mass M_{vir} , virial radius R_{vir} , halo gas mass M_{gas} and stellar mass M_* of each of the six FOGGIE galaxies analyzed in this paper at $z = 0.5$.

Halo	M_{vir} [$10^{12} M_{\odot}$]	R_{vir} [kpc]	M_{gas} [$10^{10} M_{\odot}$]	M_* [$10^{11} M_{\odot}$]
Tempest	0.43	132	1.99	0.46
Maelstrom	0.81	163	5.09	0.90
Squall	0.68	154	2.99	0.80
Blizzard	0.94	172	3.52	1.30
Hurricane	1.38	195	6.29	1.90
Cyclone	1.41	197	5.24	2.02

that resolution is concentrated where it is most physically necessary, and results in 90–99% of the CGM mass being resolved according to the cooling time criterion (R. C. Simons et al. 2020). Because the AMR scheme does not impose a minimum gas mass per cell, the median CGM cell mass in the halos studied here is $\sim 44 M_{\odot}$ and some cells reach as low as $\leq 1 M_{\odot}$ (see also C. Lochhaas et al. 2023). Similar results have been seen in an independent implementation of cooling refinement by the MEGATRON project (C. Cadiou et al. 2025). With forced and cooling refinement in place, R. C. Simons et al. (2020) could investigate the effects of highly-resolved ram-pressure stripping on dwarf satellites, and C. Lochhaas et al. (2021) could show that non-thermal, turbulent motions are a key source of dynamical support for halos that generally never reach the canonical virial temperature. R. Augustin et al. (2025) showed that small clumps are ubiquitous and often show internal ionization structure. FOGGIE methods have also been used to examine the Milky Way’s high-velocity sky (Y. Zheng et al. 2020), the assembly of the stellar halo from numerous satellites (A. C. Wright et al. 2024), the evolution of angular momentum in the CGM (R. C. Simons et al. 2024), and the stochastic variations of internal metallicity distributions (A. Acharyya et al. 2024). Basic properties of the six FOGGIE halos are given in Table 1.

The background cosmology for all simulations is a Λ CDM universe with cosmological parameters consistent with the Planck Collaboration et al. 2016 results: $\Omega_m = 0.285$, $\Omega_{\Lambda} = 0.715$, $\Omega_b = 0.0461$, $H_0 = 69.5 \text{ km s}^{-1} \text{ Mpc}^{-1}$ and $\sigma_8 = 0.82$.

The FOGGIE simulations implement simple gas physics, including radiative cooling with a self-shielding approximation for high density gas, star formation, and

Table 2. Rest-frame wavelengths and characteristic temperature ranges of emission lines analyzed in this study.^a

Line	Wavelength [Å]	Temperature [K]
H α	6563	$\sim 1 \times 10^4$
Mg II	2796	$< 5 \times 10^4$
Si II	1260	$< 5 \times 10^4$
C III	1910	$5 \times 10^4 < T < 10^5$
Si III	1207	$5 \times 10^4 < T < 10^5$
C IV	1548	$10^5 < T < 5 \times 10^5$
Si IV	1394	$10^5 < T < 5 \times 10^5$
O VI	1032, 1038	$10^5 < T < 10^6$

^aTemperature ranges are shown assuming collisional ionization.

thermal feedback from supernovae. The simulation includes metallicity-dependent cooling and a metagalactic UV background (F. Haardt & P. Madau 2012), using the Grackle chemistry and cooling library (B. D. Smith et al. 2017) with self-shielding (A. Emerick et al. 2019). Star formation occurs in gas with a comoving number density exceeding $\sim 0.1 \text{ cm}^{-3}$. The minimum star particle mass starts at $1000 M_{\odot}$ at high redshift and then ramps up to $10,000 M_{\odot}$ between $z = 1$ and $z = 2$ to reduce the total number of particles needed to simulate a Milky-Way-like host. Supernova feedback follows the implementation of R. Cen & J. P. Ostriker 2006 in which purely thermal energy is deposited into the 27 cells surrounding a star particle after 12 dynamical times have passed since its formation. Each star particle injects $1 \times 10^{-5} m_* c^2$ of energy and pushes $0.25 m_*$ of mass to the surrounding gas over 12 dynamical times following particle creation (m_* is the original star particle mass and c is the speed of light). The total metal mass ejected is calculated as $0.025 m_* (1 - Z_*) + 0.25 Z_*$ to account for metal recycling. In this method all metals are tracked as a single combined field. In this study particular elemental abundances are calculated assuming solar abundances and ion fractions and ion masses are computed using the Trident package (C. B. Hummels et al. 2017).

The main analysis of the paper has been done on CGM gas defined as all gas inside a $(100h^{-1} \text{ kpc})^3$ box, centered on the galaxy, corresponding to a 50 kpc projected distance from the galactic center. This region is smaller than the forced refinement track box and so is always resolved with cells of ≤ 732 physical pc. This

spatial extent is motivated by observational limitations: CGM emission from gas at larger distances is typically too faint to detect with current instrumentation. Additionally, our interest lies in the interface region between the galaxy and its surrounding halo, where emission is brightest and gas dynamics are most active.

2.2. Disk Removal

For some analyses we want to remove the galactic disk and focus on isolated CGM emission. This is possible in simulations because we have full the 3D density information and so can label disk and/or CGM cells on that basis. This removal is guided by observational limits on disk detection, under the assumption that disk removal from real CGM emission images can be done in a similar fashion. Figure 1 shows face-on H I column density maps for the Squall halo within a 100 kpc box. The top panel includes all gas contributing to the H I column density, while the bottom panel shows the result after removing the disk component. As described in (C. W. Trapp et al. 2025), we define the H I disk as a contiguous region with H I number density above $\sim 2 \times 10^{-2} \text{ cm}^{-3}$. To avoid missing low-density regions in the disk associated with stellar feedback or dynamical effects, we fill both fully enclosed holes and “donut” holes that completely pierce the disk. This disk removal method is based on the full 3D gas distribution in the simulation and does not depend on the chosen line of sight; it is also robust to removing misaligned disks and maintaining the disk-halo interface versus previous disk removal techniques (C. W. Trapp et al. 2025). After disk removal, some H I from in front of or behind the disk remains visible in projection within the central 20 kpc region. By subtracting the disk in this way, we focus our analysis on halo gas, isolating CGM features that are otherwise obscured by bright emission from the central disk. Figure 1 shows projected H I column density maps for Squall with and without the disk removed for comparison. Often CGM emission appears at the former disk location in projection, even with the disk removed.

2.3. Emissivity Calculation

Most of the emissivity calculations in this work follow the pipeline developed and described in detail by L. Corlies et al. (2020) and used in C. Lochhaas et al. (2025). Here, we briefly summarize the key steps involved.

In the density and temperature regimes typical of the CGM, gas cools primarily via collisional excitation followed by radiative decay. As a result, the emissivity of a given line scales approximately with the square of the gas density (n^2). The brightest emission for a given line therefore originates from gas near the temperature

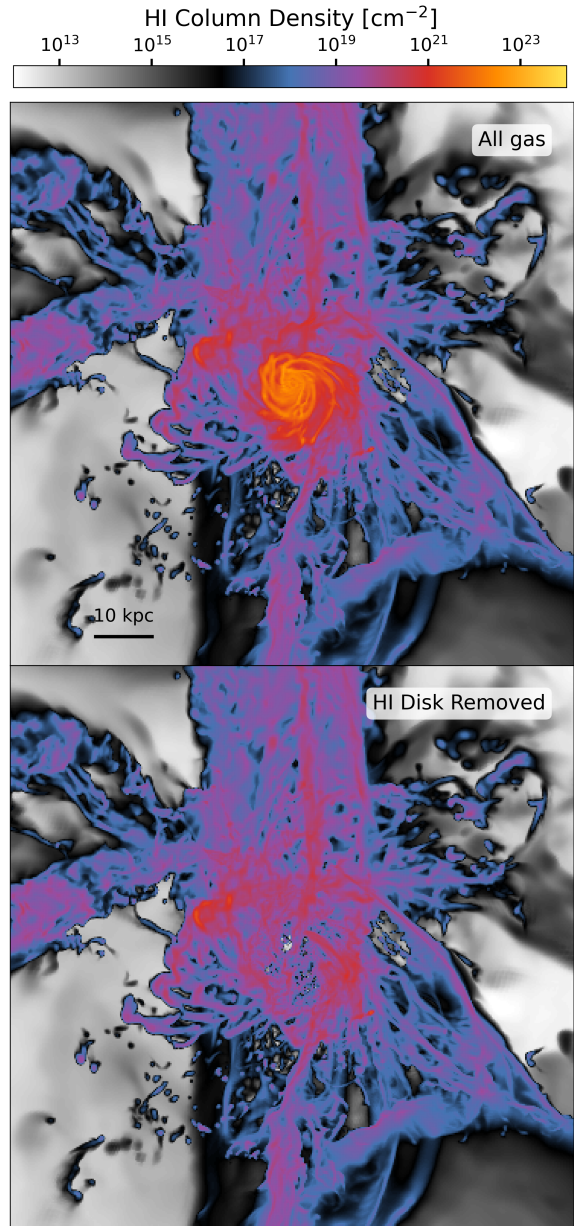


Figure 1. Face-on H I column density maps for the FOGGIE Squall halo within a 100 kpc box. *Top:* All gas contributing to the H I column density. *Bottom:* Map after removing the H I disk component. Some H I remains visible in the inner region after removing the disk; this gas is not part of the disk but lies in front of or behind it along the line of sight. This figure illustrates how removing the dense H I disk reveals surrounding gas structures and helps isolate CGM features from the disk.

at which the cooling curve peaks for that species (S. Bertone et al. 2010). To compute the line emissivity in each simulation cell, we post-process the outputs using the photoionization code CLOUDY (version 23.01; M.

Chatzikos et al. 2023). The emissivity for each line is drawn from CLOUDY tables that are parametrized by hydrogen number density (n_{H}), gas temperature (T), and redshift. These emissivities assume solar metallicity. Each metal line emissivity is then scaled linearly by metallicity of each cell, which captures the dependence on metallicity produced by the Cloudy modeling.

To begin the post processing, we first constructed CLOUDY look-up tables of emissivity as a function of temperature ($10^3 < T < 10^8$ K with steps of $\Delta \log T = 0.1$) and hydrogen number density ($10^{-5} < n_{\text{H}} < 10^2$ cm^{-3} with steps of $\Delta \log n_{\text{H}} = 0.5$) for each metal line using CIAOLOOP¹⁷ (B. D. Smith et al. 2009). Solar metallicity and abundances are assumed in these calculations.

For each cell in the simulation, we interpolate the CLOUDY grid at the cell’s temperature and hydrogen number density to obtain the emissivity value. This interpolated value is then scaled by the cell’s metallicity. We assume the gas is in ionization equilibrium and include both photo-ionization and collisional ionization processes. For the extragalactic ultraviolet background (EUVB), we adopt the F. Haardt & P. Madau (2012) model at $z = 0$, which is the same evolving UVB used during the simulation runtime. We note that the choice of UVB model can introduce inherent uncertainty in the derived ionization states; for a quantitative discussion of the uncertainties related to UVB choice refer to E. Taira et al. (2025).

Throughout this paper, we analyze emission from eight spectral lines: $\text{H}\alpha$, Mg II, Si II, Si III, C III, C IV, and O VI. We choose $\text{H}\alpha$ over $\text{Ly}\alpha$ to avoid radiative transfer effects in optically thick gas, to get results for at least one line optimized for ground-based telescopes, and in consideration of the fact that UV instruments in low-Earth orbit will likely need to avoid or suppress $\text{Ly}\alpha$ to reduce scattered light. The specific rest-frame wavelengths used for each line are listed in Table 2. All six FOGGIE halos are included in the full analysis. Figures presented in the paper are selected to be representative of the general trends observed across the full halo sample; while a single halo may be shown for illustrative purposes, the findings apply broadly and are not limited to the examples.

3. MAPPING THE CGM IN MULTIPHASE EMISSION LINES

In this section we make predictions for H I and metal line emission and demonstrate the role instrumental spa-

tial resolution and sensitivity play in detecting and understanding the CGM.

Figure 2 presents face-on surface brightness maps for eight emission lines— $\text{H}\alpha$, O VI, C IV, Si IV, C III, Si III, Mg II, and Si II—for the Squall halo. Emission from the galactic H I disk has been removed, and the green contours indicate the region where the disk was. These maps reveal a diverse range of emission morphologies across different ions, reflecting the multiphase structure of the CGM. Zoom-in panels are included to emphasize spatial differences and trace features that change significantly from one ion to another.

O VI emission, which traces warm and/or diffuse gas ($T \sim 10^{5-6}$ K), exhibits a smooth, volume-filling morphology that sets it apart from the filamentary or clumpy structures seen in lower ionization lines. Notably, the prominent extended loop seen in the $\text{H}\alpha$ zoom-in region is almost invisible in the O VI panel, emphasizing the distinct temperature and density regimes probed by these lines. Its diffuse distribution reflects its origin in lower-density, higher-temperature gas that permeates the CGM more uniformly. Interestingly, a few bright clumps of O VI emission appear in the top-left region of these O VI emission maps that are not seen in any of the lower ionization lines. These localized enhancements are unique to O VI but common in all our simulations, and may trace transient or shock-heated structures in the hotter CGM phase. The differences between the O VI distribution and that of lower ions can play a key role in determining the nature of the gas in the CGM (M. Tcoras et al., in prep).

Moving to slightly lower ionization states, C IV and Si IV begin to trace some of the filamentary features seen in $\text{H}\alpha$. C IV shows both diffuse and structured emission, partially recovering the loop feature. Si IV, while overall fainter, reveals the loop shape even more clearly, suggesting that it arises in gas at intermediate temperatures between the C IV and $\text{H}\alpha$ phases.

The intermediate ions C III and Si III also show interesting differences. The structures in C III appear larger and more diffuse than in Si III. For instance, while the loop structure is easier to recognize in C III than in C IV, the clumpy emission above the loop appears more extended and blurred compared to the sharper, more compact structures in Si III. These differences trace subtle variations in gas density and temperature that affect emission from these two ions differently.

At the lowest ionization levels, Mg II and Si II show emission patterns more closely aligned with the $\text{H}\alpha$ distribution. However, important differences persist. For example, in the zoomed region, both Mg II and Si II trace parts of the loop seen in higher ions, but Mg II

¹⁷ https://github.com/brittonsmith/cloudy_cooling_tools.git

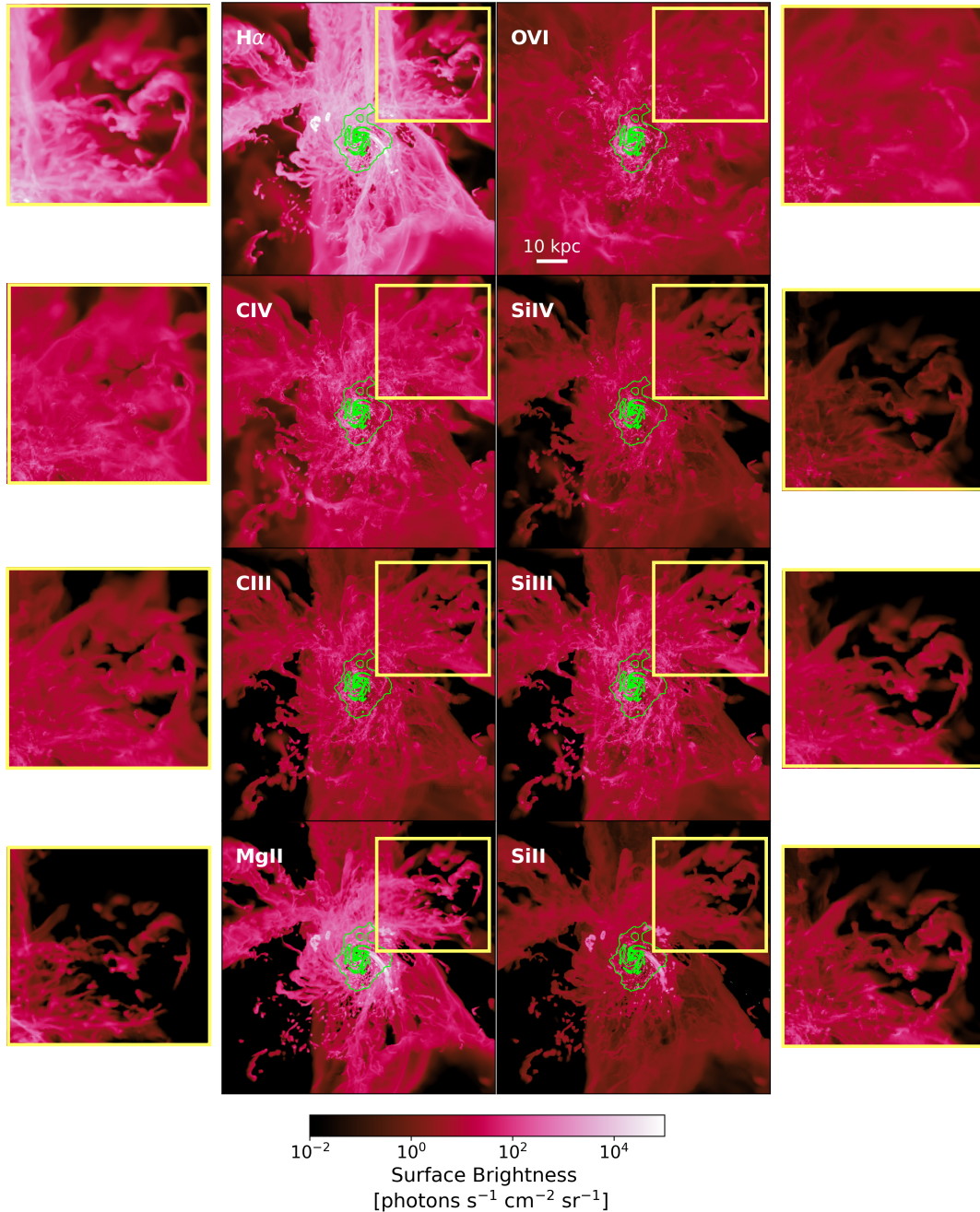


Figure 2. Face-on surface brightness maps of the Squall halo for eight ions with emission lines in the UV/optical: $H\alpha$, Mg II, Si II, Si III, C III, C IV, and O VI.. The box sizes cover 100 kpc fields of view. The H I disk has been removed to isolate CGM emission; green contours indicate where the disk was. These maps highlight the multiphase nature of the CGM, as different ions trace different physical structures and temperatures. The zoom-in panels emphasize key differences in morphology across ions. These comparisons demonstrate that no single emission line fully captures the CGM’s complexity. Each ion offers a distinct view of its structure and thermodynamic state. Observing multiple UV lines is essential for building a complete, multiphase picture of the circumgalactic medium.

displays distinct clumps in the region where the $H\alpha$ map shows a loop. On the right side of the disk, a filament visible in Si II extends to the edge of the map, whereas in Mg II it is truncated. These differences illustrate how

even among low-ionization species, emission structure can vary depending on local gas properties.

Together, these maps demonstrate the value of observing the CGM in multiple UV emission lines. Each ion

captures a different phase of the gas - ranging from hot and diffuse to cool and dense - and only by combining them can we build a comprehensive, multiphase picture of CGM structure and physical conditions.

Figure 3 presents radial surface brightness profiles for all eight emission lines analyzed in this study. Each panel shows the median surface brightness as a function of R/R_{vir} , computed across all six FOGGIE halos. Solid lines represent profiles including all gas (disk and CGM), while shaded regions indicate the scatter among halos. Dashed lines show the profiles after removing the H I disk, isolating the CGM contribution. Note that in the CGM surface brightness profiles, only the galactic disk is removed; satellite galaxies are still included as part of the CGM. Removing satellites produces only minor changes to the profiles and does not affect our results.

Most ions (e.g., O VI, C IV, Si IV, C III, Si III) exhibit smooth power-law profiles extending from the halo outskirts inward. In contrast, H α , Mg II, and Si II show a clear transition in slope around $R \sim 0.1 R_{\text{vir}}$: from a steep power-law decline at large radii to an exponential rise toward a central plateau. This broken profile is consistent with recent observational findings by [N. M. Nielsen et al. 2024](#) for [OII] and [OIII] and reflects the transition between CGM and disk-dominated emission. After H I disk removal, the central region becomes flattened for low-ionization lines, confirming that the steep inner profiles are driven by disk emission. These results support the interpretation that breaks in radial surface brightness profiles of lower ions mark a structural transition between CGM and galactic disk. The profiles also recall the findings of the AMIGA absorption line survey of M31, which found enhancements in low ions as sight-lines approach the disk that are not reflected in the high ions ([N. Lehner et al. 2025b](#)).

4. ESTIMATING THE CGM MASS IN EMISSION

A complete understanding of the CGM requires observations across a wide range of low to high ionization states, each tracing different temperatures, densities, and spatial morphologies. In this section, we focus on the observability of these emission lines and examine how instrumental limitations, specifically spatial resolution and sensitivity, impact our ability to detect and map CGM gas in practice. All analysis has been done for the CGM after removing the H I disk¹⁸.

We begin by presenting edge-on surface brightness maps for the Blizzard halo in Figure 4, for three representative UV emission lines, O VI, C III, and Mg II,

capturing a wide range of CGM gas phases. O VI traces warm-hot diffuse gas ($T \sim 5 \times 10^5$ K), C III traces intermediate temperature gas ($T \sim 5 \times 10^4$ K), and Mg II traces the cold gas ($T \sim 10^4$ K). While this figure focuses on one halo for illustration, the full analysis has been performed across all FOGGIE halos and eight emission lines, with consistent results. Throughout the paper, we select specific halos for display based on their clarity and the degree to which they are representative of patterns in the full set; these choices are made solely for illustrative purposes, such as when the viewing angle significantly affects the interpretation. The edge-on orientation is chosen here to better reveal the CGM structures surrounding the galaxy.

In Figure 4 each row corresponds to a different ion, while each column represents increasing spatial resolution: 0.27 kpc, 1 kpc, 3 kpc, and 6 kpc. These correspond at $z = 0.5$ ($z = 0, 10$ Mpc) to approximately 0.04 (5.6), 0.16 (20), 0.5 (61), and 1 (120) arcseconds, respectively. The galactic disk has been excluded from all panels to focus on CGM emission. The colormap represents surface brightness in units of photons $\text{s}^{-1} \text{cm}^{-2} \text{sr}^{-1}$. Pixels below 100 photons $\text{s}^{-1} \text{cm}^{-2} \text{sr}^{-1}$ threshold appear in grayscale, while colored pixels indicate detectable emission. These thresholds mimic the sensitivity of current and possible future UV instruments.

At a sensitivity of > 100 photons $\text{s}^{-1} \text{cm}^{-2} \text{sr}^{-1}$ (corresponding to regions shown in blue, purple, and yellow), extended CGM structures such as filaments and streams are visible out to distances of ~ 50 kpc in all three ions in the highest resolution column. These features are preserved at 1 kpc resolution but begin to disappear at coarser resolutions as the brighter regions are averaged down with fainter areas. This fading occurs because their surface brightness is only slightly above the sensitivity threshold - around 100 photons $\text{s}^{-1} \text{cm}^{-2} \text{sr}^{-1}$, and they are surrounded by regions with much lower surface brightness. As the pixel size increases, each pixel averages over a larger area. This means bright regions are blended with adjacent, fainter regions. Although the total number of photons within a larger pixel may increase, the surface brightness (i.e., photons per unit area) often decreases, because the increase in area outweighs the gain in photon counts. If a large pixel includes more faint gas than bright gas, the surface brightness of that pixel may drop below the instrument's detection limit—causing previously visible structures to vanish in the map.

At a higher threshold of ~ 500 photons $\text{s}^{-1} \text{cm}^{-2} \text{sr}^{-1}$ (purple and yellow), the extended CGM structures are no longer visible. An instrument limited to this sensitivity would primarily detect the denser regions near

¹⁸ Gas outside the 3D disk can still appear in projection at the disk's former location.

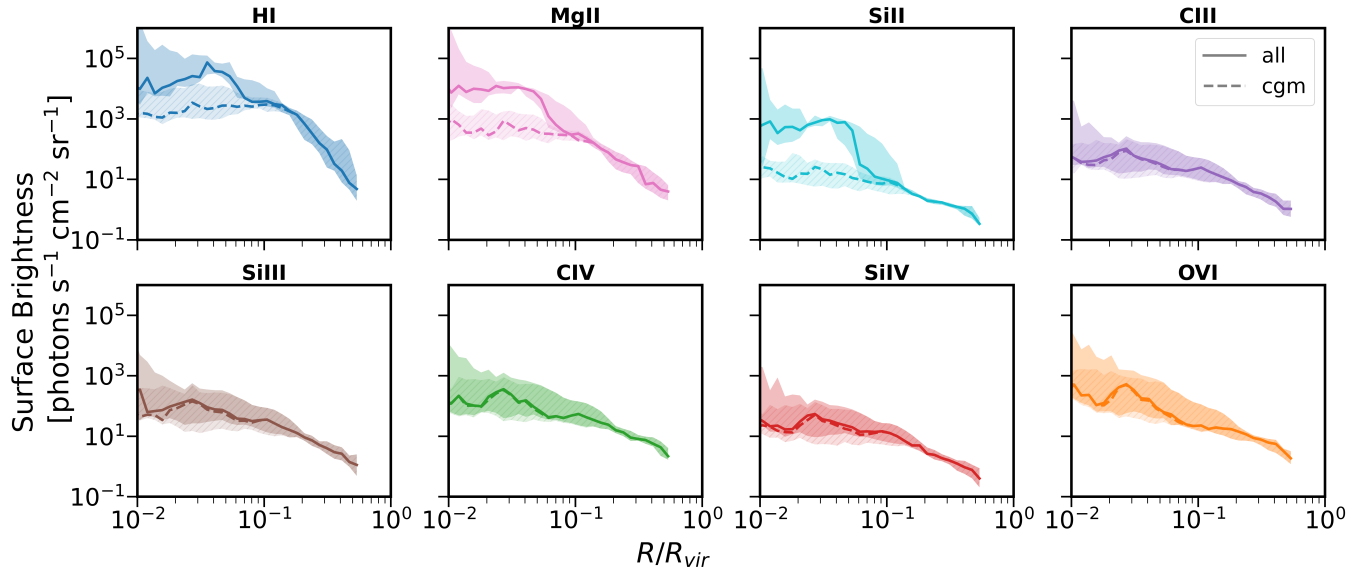


Figure 3. Radial surface brightness profiles for eight ions across all FOGGIE halos (face-on, 0.27 kpc resolution). Solid lines show median profiles including all gas; dashed lines show CGM-only emission after H I disk removal. Shaded regions indicate the range of halo-to-halo variation. Most ions follow power-law profiles, while H α , Mg II, and Si II show a break in slope around $0.1 R_{\text{vir}}$ —reflecting a transition from disk to CGM-dominated emission. CGM-only profiles flatten at small radii for low-ionization species.

the galaxy center. At the highest resolution, some features can still be seen around the central region. For Mg II, extended bright structures out to ~ 30 kpc remain detectable at this threshold, whereas intermediate ions such as C III are fainter and show less extended structure beyond the center. Comparable structures are visible at 1 kpc resolution, though much of the fine detail disappears by 3 kpc, even though the radial extent of detection remains similar to the 0.27 kpc maps. At the poorest spatial resolution of 6 kpc, only a handful of bins are detectable. At this scale, detailed structures vanish entirely, but the overall radial extent of the detectable emission remains comparable to that seen at very high spatial resolution.

At a sensitivity threshold of $2000 \text{ photons s}^{-1} \text{ cm}^{-2} \text{ sr}^{-1}$ (yellow), the detectable O VI emission is similar to that at $500 \text{ photons s}^{-1} \text{ cm}^{-2} \text{ sr}^{-1}$ for the 0.27 and 1 kpc maps. However, in the lower-resolution maps (3 and 6 kpc), detection is restricted to very small, bright clumps near the galactic center. The same trend is seen for C III. In contrast, the extent of Mg II emission changes significantly between sensitivities of 500 and $2000 \text{ photons s}^{-1} \text{ cm}^{-2} \text{ sr}^{-1}$: at 2000, detectable emission is limited to the central regions. At coarse resolutions of 3 and 6 kpc, only a few pixels remain above the detection threshold.

In addition to how structure and extent of detectable ions change by changing sensitivity and spatial resolution of an instrument, we can also explore the amount of mass that is observable. Figure 5 presents heatmaps of the observable CGM mass fraction for the same representative ions: O VI, C III, Mg II; the heat map for all eight emission lines: H α , O VI, C IV, Si IV, C III, Si III, Mg II, and Si II can be found in Appendix B. The mass of each ion is computed using TRIDENT (C. B. Hummels et al. 2017). These maps indicate the fraction of CGM by mass that is emitting in each line that would be detectable within a 100 kpc field of view. The analysis uses an edge-on projection and the values are averaged over all six halos. The general trends described below hold for individual halos and for face-on projections (see Figure 16 in Appendix B). Each panel shows the percentage of each ion’s mass in the CGM that would be detectable by an instrument with a given combination of surface brightness sensitivity (y-axis, in $\text{photons s}^{-1} \text{ cm}^{-2} \text{ sr}^{-1}$) and spatial resolution (x-axis, in kpc). The values are color-coded and also explicitly labeled in each cell.

The observable mass fraction decreases toward the upper-right corner of each panel, i.e., under conditions of low sensitivity and coarse resolution. At fixed sensitivity (e.g., $100 \text{ photons s}^{-1} \text{ cm}^{-2} \text{ sr}^{-1}$), changing the spatial resolution from 0.27 to 6 kpc leads to a gradual

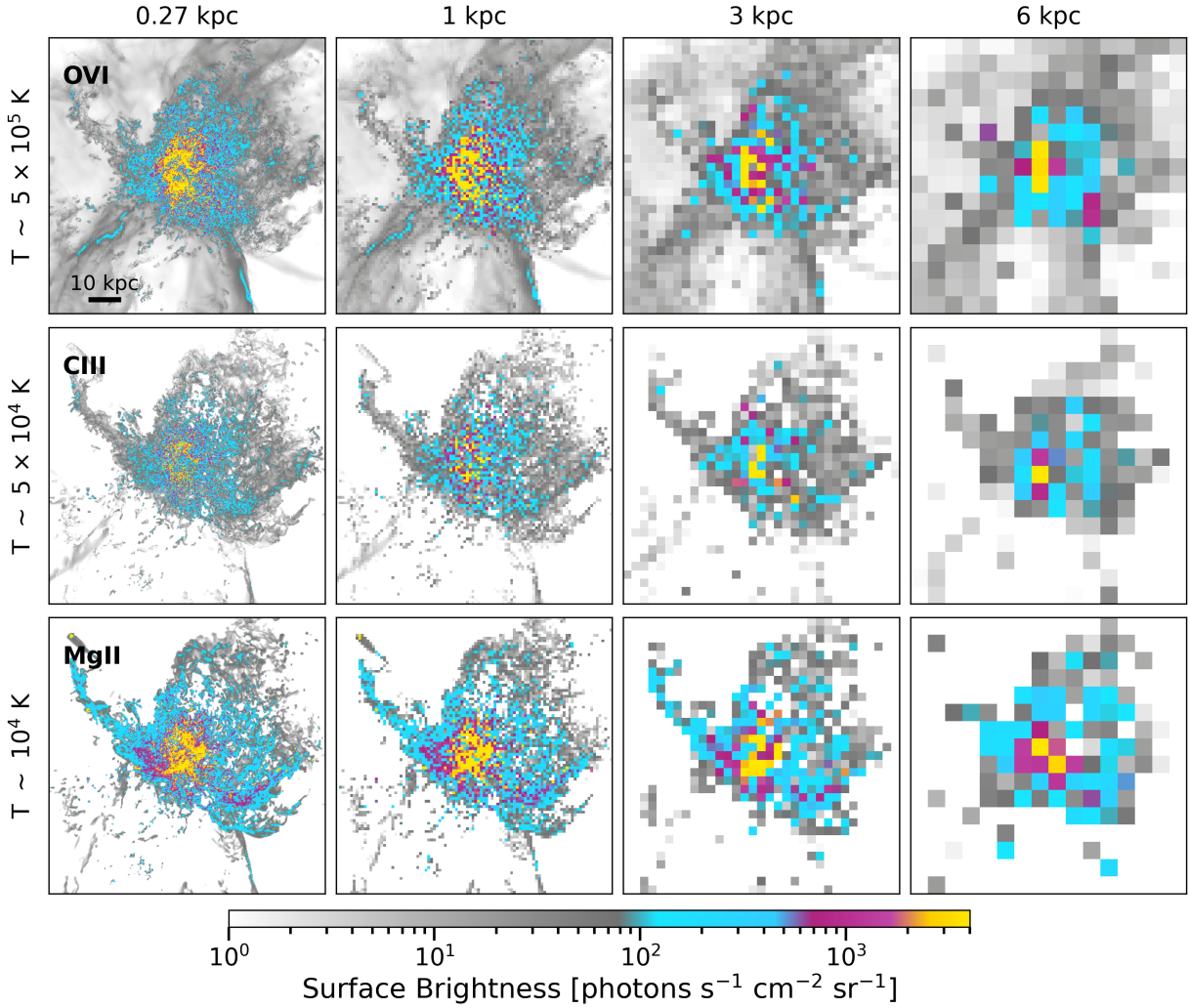


Figure 4. Surface brightness maps for three UV emission lines for the Blizzard halo, shown edge-on. Each column corresponds to a different spatial resolution: 0.27 kpc, 1, 3 and 6 kpc. These correspond at $z = 0.5$ ($z = 0, 10$ Mpc) to ~ 0.04 (5.6), 0.16 (21), 0.5 (62), and 1 (123) arcsec, respectively. The galactic disk has been removed to isolate CGM emission. The colormap represents surface brightness in units of $\text{photons s}^{-1} \text{cm}^{-2} \text{sr}^{-1}$, with grayscale indicating regions below a representative instrument sensitivity threshold. Colored regions are potentially detectable by instruments with corresponding sensitivity. For reference, at $z = 0.5$, 6 kpc subtends ~ 1 arcsec, similar to the limits of seeing-limited ground-based observations, while a space-based telescope or AO-assisted ground-based telescope could reach ~ 0.1 arcsec, or $\lesssim 1$ kpc spatial resolution.

reduction in observable mass, but this decline is modest for most ions. In contrast, at fixed resolution (e.g., 1 kpc), changing the sensitivity limit from 100 to 500 $\text{photons s}^{-1} \text{cm}^{-2} \text{sr}^{-1}$ results in a much steeper drop in detectable mass, especially for ions tracing hotter, more diffuse phases such as O VI.

To further quantify the effects of sensitivity and spatial resolution on CGM detectability, we fit a simple power-law model to the observable mass fraction,

$$f(x, y) = ax^b y^c, \quad (1)$$

where $f(x, y)$ is the fraction of CGM mass observable in a given ion, x is the spatial resolution, and y is the

surface brightness sensitivity. The exponents b and c represent how strongly each parameter influences detectability: higher values indicate that small changes in that parameter produce larger changes in observable mass.

Figure 6 presents the best-fit values of b and c for each ion. In all cases, the sensitivity exponent c is larger than the spatial resolution exponent b , indicating that sensitivity has a stronger impact on CGM observability. The fitting function reproduces the heatmap values with a mean absolute error (MAE) $\leq 7\%$ for each ion, demonstrating the robustness of the model.

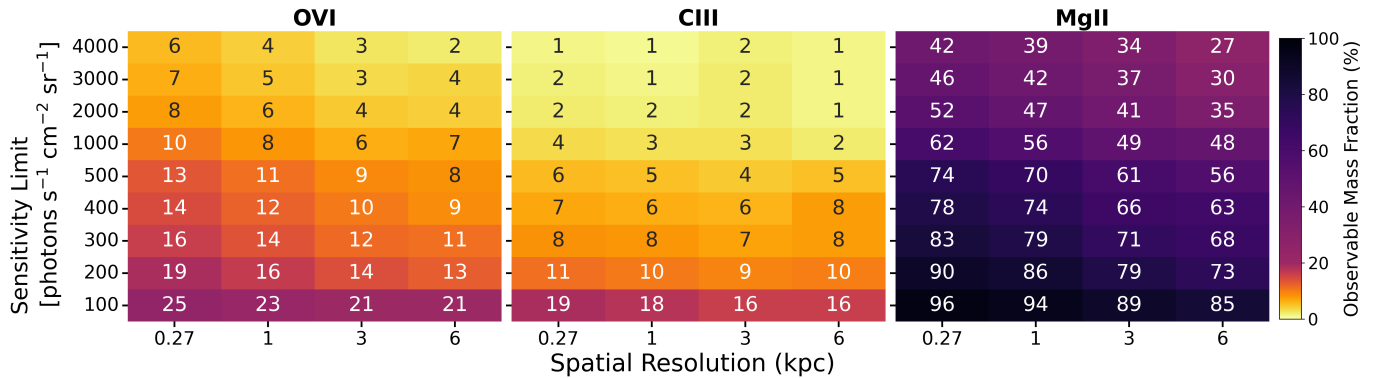


Figure 5. Observable CGM mass fraction as a function of spatial resolution (x-axis) and surface brightness sensitivity (y-axis). The spatial resolutions of 0.27, 1, 3, and 6 kpc, correspond at $z = 0.5$ ($z = 0, 10$ Mpc) to ~ 0.04 (5.6), 0.16 (20), 0.5 (61), and 1 (120) arcsec, respectively. These maps are for three representative emission lines, averaged over six FOGGIE halos and for edge-on projections (see Appendix B for maps of all eight ions’ face-on and edge-on results). Each cell shows the percentage of total CGM mass detectable above the given sensitivity limit at the specified resolution, with values color-coded and overlaid. As expected, observability decreases with lower sensitivity and coarser resolution, though sensitivity plays a stronger role: at fixed resolution, increasing the detection threshold from 100 to 500 reduces the detectable mass by more than 50% in several ions. Achieving high sensitivity is critical for maximizing CGM detection, particularly for tracing diffuse, highly ionized gas.

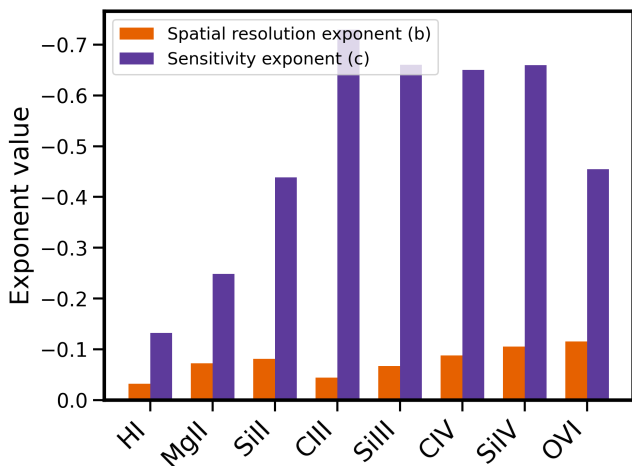


Figure 6. Spatial resolution exponent (b) and sensitivity exponent (c) from the fitting formula (Eqn. 1). A larger value of the sensitivity exponent indicates a stronger influence of sensitivity on recovering the CGM mass for each ion.

These results highlight the need for emission mapping instruments to prioritize sensitivity—particularly below the $500 \text{ photons s}^{-1} \text{ cm}^{-2} \text{ sr}^{-1}$ threshold—to maximize the detection of CGM emission across a wide range of ionization states. Sensitivity gains are especially critical for uncovering the more diffuse and extended components of the warm-hot CGM traced by higher ions.

It is important to note that the observable emission-line strengths presented in this section are likely lower limits. The FOGGIE simulations at some stages of their evolution under-predict column densities of these ions by ~ 1 –2 dex compared to quasar absorption line observa-

tions (e.g., J. Tumlinson et al. 2011; N. Lehner et al. 2020). Since emission scales with density, the resulting surface brightness—and thus the inferred detectable mass—may also be underestimated by a similar amount. This discrepancy could arise from several factors, including lower simulated CGM densities or metallicities, differences in temperature structure, or missing physical processes such as AGN-driven ionization (see also A. C. Wright et al. 2024 for a thorough discussion of FOGGIE’s current star formation and feedback implementations). Therefore, while these maps and fits provide useful insight into how instrument parameters shape detectability, the absolute values of observable CGM mass fractions should be interpreted as lower bounds rather than precise predictions. Relative comparisons (FOGGIE-to-FOGGIE) can be considered reliable, but may be discrepant with findings from other simulations. In any case our finding that sensitivity plays a more dominant role than spatial resolution remains robust and is independent of the specific column density normalization in FOGGIE.

5. RESOLVING CGM KINEMATICS IN EMISSION

5.1. Separating Different Gas Phases

Advancing our understanding of the CGM requires more than just detecting its structures; we must also disentangle its dynamics. In this section, we focus on the instrument capabilities necessary to resolve the kinematics of gas inflow and outflow around galaxies.

In this analysis and discussion, we will consider both “kinematic” resolution and “spectral” resolution as distinct concepts. The latter generally refers to a fixed

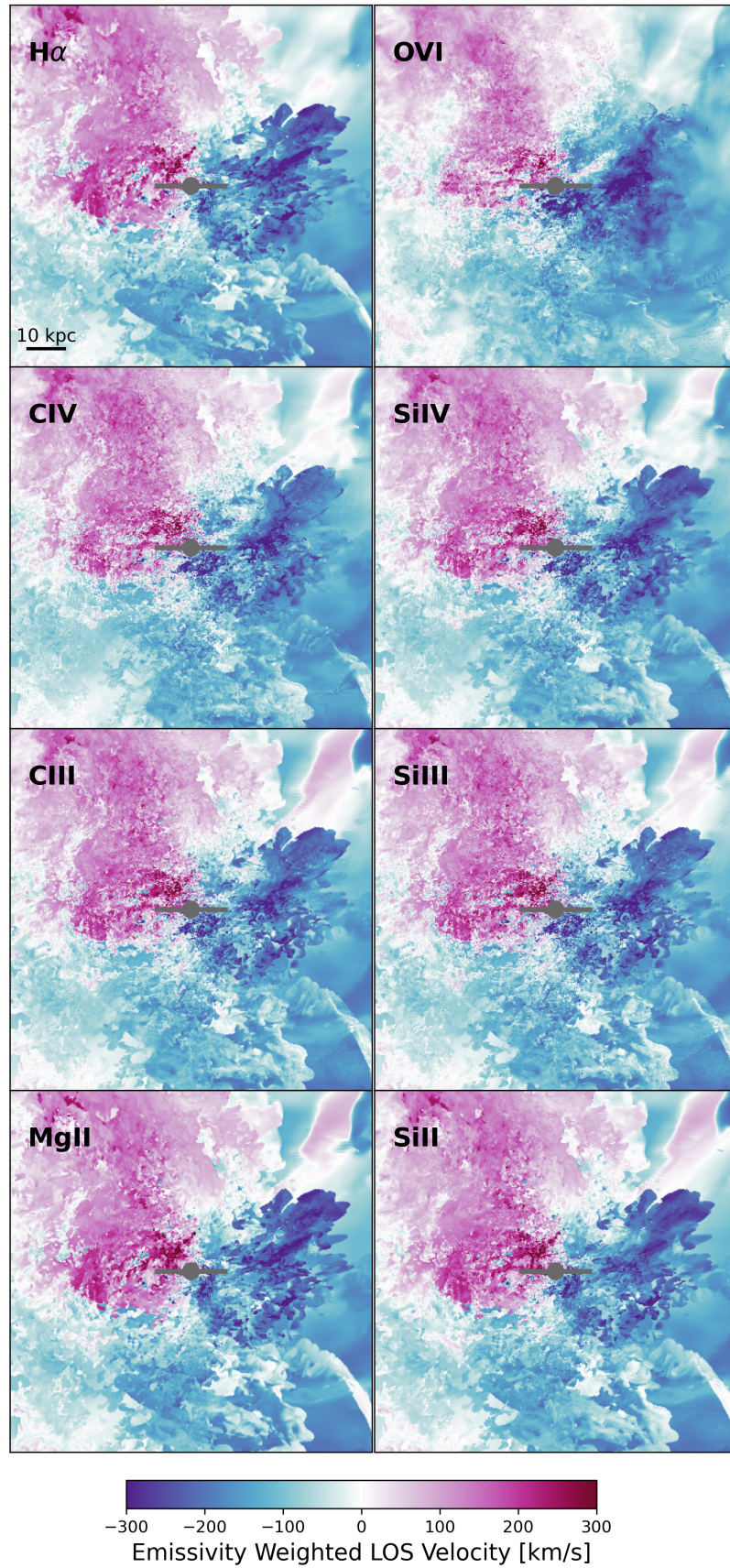


Figure 7. Emissivity-weighted projected line of sight velocity maps for eight ions for the Cyclone halo in an edge-on view and a field of view of 100 kpc. The galactic disk has been removed in all panels to isolate the kinematics of CGM gas. The gray line shows where the disk was.

property or specification of an instrument, which is generally expressed as R , and defined as $R = \lambda_0/\Delta\lambda$ for a line at wavelength λ_0 observed with a dispersion of $\Delta\lambda$. For a real instrument, this quantity can vary with wavelength or across a field of view, but generally does not vary from observation to observation. By contrast, we use “kinematic resolution” to describe the final, delivered velocity separation between two components that can be reliably distinguished in a final, reduced dataset. Unlike “spectral resolution”, which is a specification of the instrument, kinematic resolution depends on properties of the observation such as noise, instrumental broadening, intrinsic non-Gaussian line profiles, or other unknown effects. In many observations the relevant spectral and kinematic resolution will be similar, but we maintain the distinction in any case to retain the idea that our analysis relates more closely to the final, delivered kinematic resolution and not the original instrument specification.

In making these simulated maps at different spatial resolutions, we have not accounted for realistic image performance or point-spread functions (PSFs) which should vary widely from instrument to instrument or even across a field in a single instrument. Instead we study the idealized maps resampled with varying levels of binning or pixelation. To simulate a particular instrument’s real performance we would need to convolve these maps with a PSF that depends on wavelength, field position, and other properties, and resample, but this complication is beyond the scope of our current investigation. For present purposes the “spatial resolution” here is only an approximation to real instrument performance.

Figure 7 shows projected maps of the emissivity-weighted average velocity along line of sight for eight ions: H α , O VI, C IV, Si IV, C III, Si III, Mg II, and Si II for the Cyclone halo in an edge-on view. The galactic disk has been removed, as described in Section 2, in all panels to isolate the kinematics of the CGM. The gray horizontal line shows where the disk was.

A general trend across all ions is the transition from blue to pink in the projected maps, indicating large-scale radial rotation of gas around the galactic center. This pattern is highlighted by the choice of an edge-on viewing angle. Although these maps reveal broad velocity structures and trends, distinguishing differences between ions by eye is challenging. Nevertheless, some patterns emerge. High-ionization species such as O VI exhibit relatively smooth velocity gradients, consistent with diffuse, large-scale flows, such as the inflows that C. Lochhaas et al. (2025) finds that O VI emission tends to trace. In contrast, lower-ionization lines like Mg II and

Si II trace more irregular, small-scale velocity structures, often associated with clumps and filaments (see also R. Augustin et al. 2021). Other ions such as C IV, Si IV, and C III show a mix of these patterns, highlighting their role in bridging different thermal phases.

To quantify the kinematic differences between gas traced by different lines, Figure 8 presents a detailed comparison between the projected velocities of H I and three representative species (O VI, C III, and Mg II) and examines how the ability to distinguish these differences depends on spectral resolution of an instrument. We start by explaining the top three: the plots in these rows show spatial maps of absolute line-of-sight velocity differences between H I and the other ions (row 1: H I–O VI, row 2: H I–C III, row 3: H I–Mg II). These maps are computed by subtracting the H I projected velocity map from the projected velocity map of each ion on a pixel-by-pixel basis, and taking the absolute value. Each column corresponds to a different kinematic resolution: 200 km s⁻¹, 100 km s⁻¹, and 30 km s⁻¹. Colored pixels indicate regions where the velocity difference exceeds the resolution threshold and would therefore be distinguishable by an instrument that achieves that kinematic resolution, while gray pixels mark unresolved regions. The percentages on the top left show how much of the surface area in each map is resolved. These resolved percentages are shown for all six FOGGIE halos in Figure 9.

The comparison reveals that velocity differences between H I and O VI are the largest among the three ion pairs. Even at 200 km s⁻¹ resolution, as shown in Figure 9, a larger portion of the CGM shows resolvable differences between H I and O VI compared to other ions. This reflects the fact that O VI primarily traces hot, diffuse gas (C. Lochhaas et al. 2025) with distinct kinematic behavior from the colder structures traced by H I. In contrast, C III shows smaller differences from H I, with only limited areas resolvable at 200 km s⁻¹, and broader coverage at 100 km s⁻¹ and 30 km s⁻¹. The H I–Mg II pair shows the smallest differences; even at 30 km s⁻¹ resolution, less than 30% of the mass is resolved (see right panel of Figure 9), indicating that these ions are correlated and trace similar cold gas structures with nearly identical kinematics. To resolve more than 60% of the map area for H I–Mg II, kinematic resolution finer than 5 km s⁻¹ would be required.

The bottom panel of Figure 8 shows normalized emissivity vs line-of-sight velocity for illustrative lines of sight (highlighted in green in the top maps). Each column corresponds to one kinematic resolution bin (200, 100, and 30 km s⁻¹ from left to right), while each row compares H I (blue) to O VI (orange), C III (green),

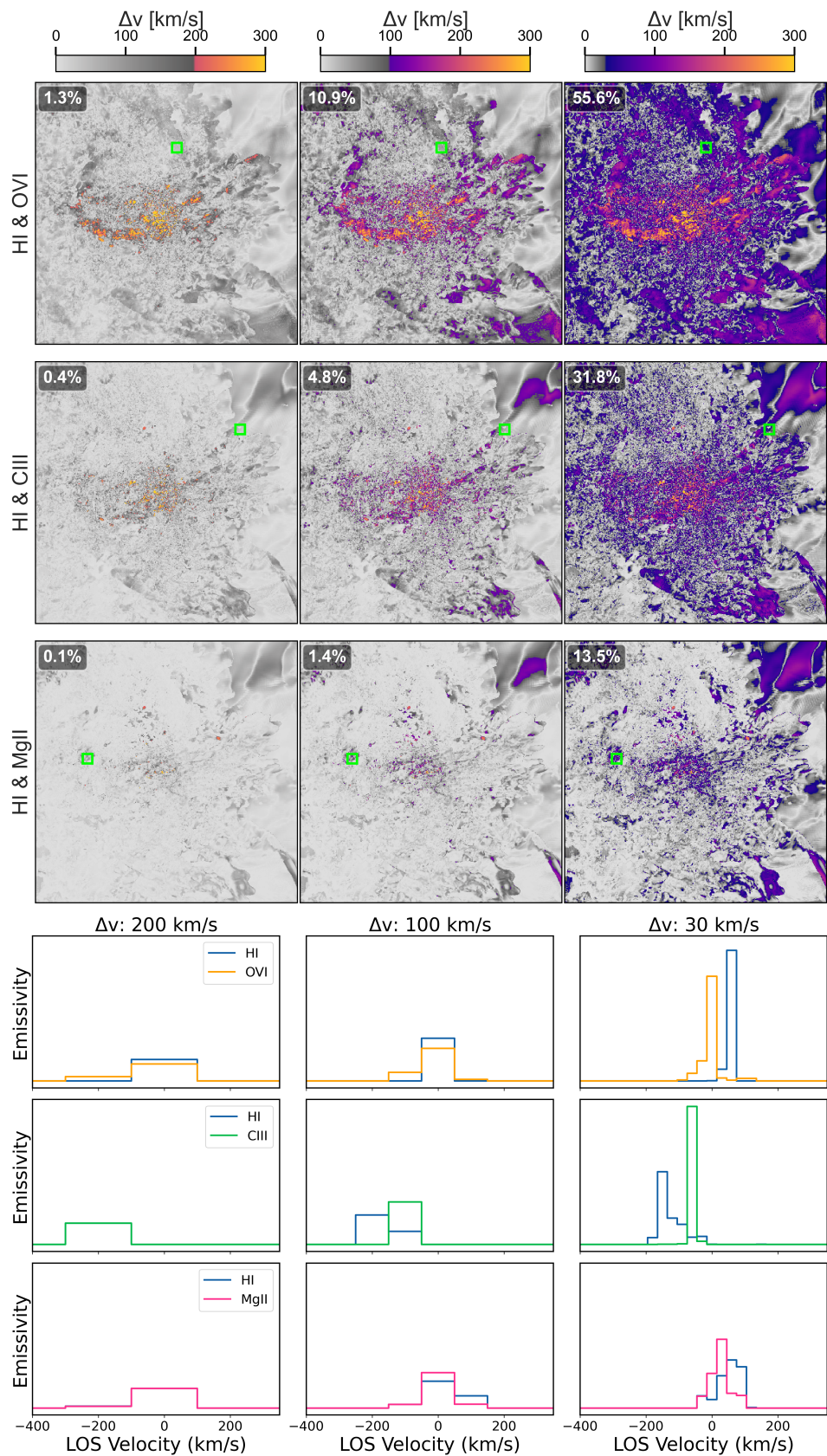


Figure 8. Velocity differences between H I and O VI, C III, and Mg II in the Cyclone halo. *Top:* Maps show where emissivity-weighted velocity differences exceed kinematic resolution thresholds (200, 100, 30 km s⁻¹). Gray pixels are unresolved; colored pixels are kinematically distinguishable. Percentages in the top-left of each panel indicate the fraction of the area with resolved kinematic differences (i.e., colored pixels divided by total area). *Bottom:* Normalized velocity profiles along the selected sightlines (marked by green boxes in the top panels). Each column corresponds to the same sightline across resolution levels. These profiles highlight how improved spectral resolution enables clearer separation between the velocity structures of different ions.

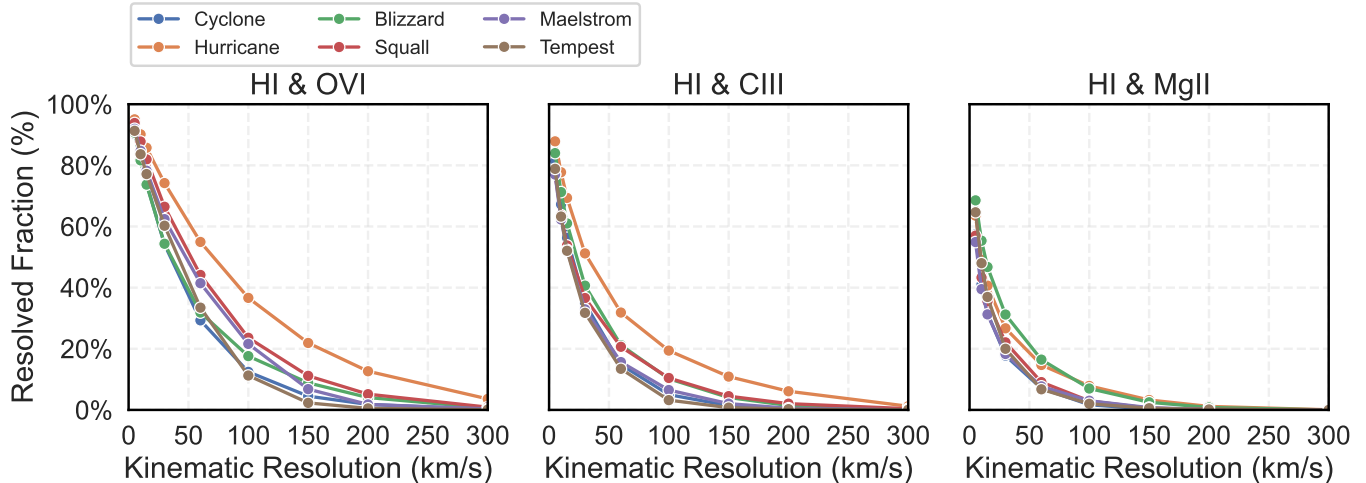


Figure 9. Resolved fraction of CGM surface area as a function of kinematic resolution for velocity differences between H I and three representative ions: O VI (left), C III (middle), and Mg II (right). Each line corresponds to one of the six FOGGIE halos. The resolved fraction indicates the percentage of pixels where the velocity difference between the two ions exceeds the given resolution threshold and would therefore be distinguishable by an instrument. O VI shows the largest kinematic differences from H I. C III requires finer resolution ($< 30 \text{ km s}^{-1}$) for broad coverage, while Mg II remains largely unresolved even at 30 km s^{-1} , reflecting its close kinematic alignment with H I.

and Mg II (pink), respectively. At 200 km s^{-1} resolution, the velocity profiles for H I and the comparison ion are nearly indistinguishable in each case, therefore they are shown in grey color. However, as the resolution improves to 100 and then 30 km s^{-1} , distinct features emerge in the profiles, especially for O VI and C III. The Mg II and H I profiles remain closely aligned even at the highest resolution, reinforcing the result that these ions share tightly coupled kinematics; R. Augustin et al. (2025) also show that the gas traced by these ions is closely aligned spatially.

Figs. 8 and 9 emphasize the critical role of kinematic resolution in disentangling the kinematics of the multi-phase CGM. High-ionization species like O VI exhibit distinct velocity structures compared to neutral hydrogen, while lower-ionization lines such as Mg II often trace cold gas dynamics very similar to H I. The ability to resolve these differences depends strongly on instrumental resolution: coarse resolutions obscure important velocity offsets, especially between phases, whereas finer resolutions are necessary to capture the diversity of motions across ionization states. These results underscore that recovering the full kinematic picture of the CGM requires not only spatial mapping but also sufficient kinematic precision to separate the dynamics of different phases.

5.2. Separating Inflow From Outflow From Disk

Beyond distinguishing between different ionization phases, resolving CGM kinematics is also essential for

uncovering the underlying motions of the gas like disentangling inflowing gas from outflowing gas. One of the persistent challenges in interpreting CGM observations is separating these opposing gas motions along the line of sight. High kinematic resolution offers a pathway to tackle this challenge by capturing the subtle velocity differences.

To explore this further, we leverage the full 3D velocity information available in the simulations to define inflow and outflow in the CGM. We define inflow as gas with a 3D radial velocity $v_{\text{rad}} \leq -100 \text{ km s}^{-1}$ and outflow as gas with $v_{\text{rad}} \geq 200 \text{ km s}^{-1}$. The inflowing velocity cut of -100 km s^{-1} captures gas moving at at least one-third of the free-fall velocity within 50 kpc of the galaxy centers in the halos studied here, while the outflowing velocity cut of 200 km s^{-1} approximately corresponds to the escape velocity for these halos. These cuts are chosen to isolate coherent radial flows rather than turbulent or random gas motions (C. Lochhaas et al. 2021).

The top two panels of Figure 10 present emissivity-weighted projected velocity maps for O VI in the Maelstrom halo viewed edge-on. The left panel includes only gas classified as inflow, while the right panel includes only outflowing gas. In both projections, only gas meeting the respective inflow or outflow criteria contributes to the emissivity-weighted velocity at each pixel.

The bottom-right panel of Figure 10 shows the pixel-by-pixel difference between these two velocity maps. Specifically, each pixel in this grayscale map represents the difference between the emissivity-weighted line-of-

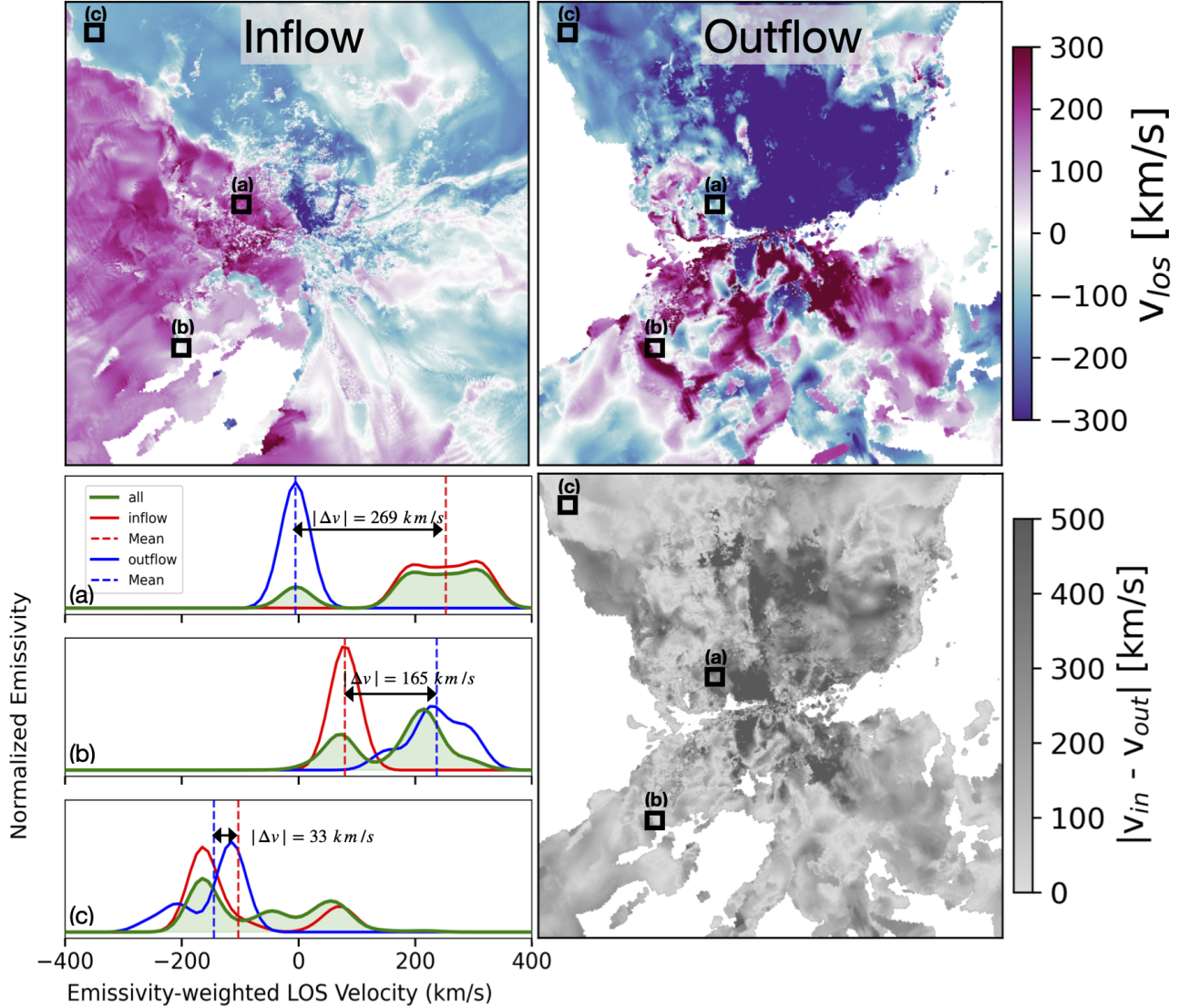


Figure 10. Top panels: Emissivity-weighted line-of-sight velocity maps for O VI in the Maelstrom halo (edge-on view), showing only gas classified as inflow (with a center-directed $v_{\text{rad}} \leq -100 \text{ km s}^{-1}$ in the frame of the galaxy’s center of mass; left panel) or outflow ($v_{\text{rad}} \geq 200 \text{ km s}^{-1}$; right panel), based on 3D radial velocities. Bottom left panels (a, b, c): Emissivity-weighted line-of-sight velocity profiles for three selected sightlines (black squares labeled a–c in the top and bottom maps), showing distributions for all gas (green), inflowing gas (red), and outflowing gas (blue). Dashed lines mark the emissivity-weighted mean velocity of each component. The labeled $|\Delta v|$ indicates the absolute difference between the inflow and outflow mean velocities along each sightline. Bottom-right: Grayscale map showing the absolute difference in emissivity-weighted projected velocity between inflow and outflow at each pixel. This figure illustrates the kinematic signatures of inflowing and outflowing gas, with velocity separations ranging from tens to hundreds of km s^{-1} .

sight velocity of outflowing gas and that of inflowing gas at the same location. Darker shades correspond to larger differences in projected velocity between the two components. To help interpret these differences, the bottom-left panel shows three example lines of sight (labeled a, b, c). For each one, the sub-panels illustrate several components: the green histogram shows the velocity distribution of all CGM gas along that sightline (before any classification); the red curve shows the emissivity-

weighted velocity distribution of inflowing gas¹⁹; and the blue curve shows the same for outflowing gas. The dashed vertical lines mark the emissivity-weighted *mean* velocities of the red and blue components, respectively. The absolute difference between these two mean values

¹⁹ Note that the inflow and outflow are defined using 3D velocity information.

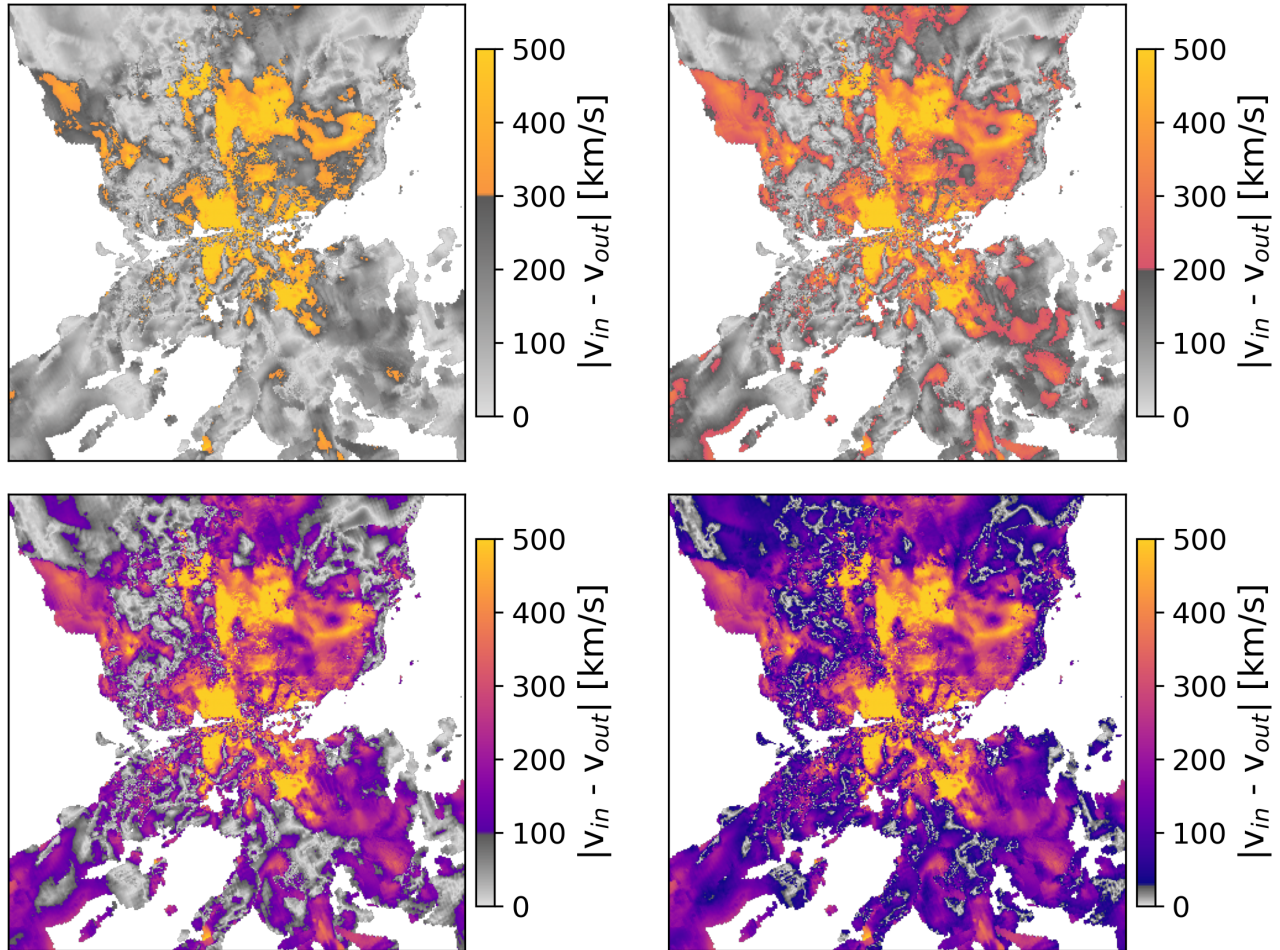


Figure 11. Projected velocity maps for inflowing and outflowing O VI-emitting gas in the Maelstrom halo (edge-on). Each panel shows the same projected map of pixel-by-pixel velocity differences between inflowing and outflowing O VI-emitting gas in the Maelstrom halo (as in the bottom-right panel of Figure 10), but filtered by different kinematic resolution thresholds: 300, 200, 100, and 30 km s⁻¹ (top-left to bottom-right). The grayscale background represents the full $|\langle v_{in} \rangle - \langle v_{out} \rangle|$ values. Colored pixels highlight regions where the velocity difference exceeds the corresponding kinematic resolution, indicating that an instrument with that velocity resolution could distinguish inflow from outflow in those areas. Gray regions fall below the resolution threshold and would be kinematically unresolved. The maps demonstrate that increasingly finer kinematic resolution enables inflow–outflow separation across larger fractions of the halo, emphasizing the importance of ≤ 30 km s⁻¹ velocity resolution for resolving CGM gas flows in emission.

is reported directly on the panel (e.g., $|\Delta v| = 269$ km s⁻¹ for line of sight “a”), and corresponds to the value shown in the grayscale map at the same location. Together, these panels highlight how kinematically distinct inflowing and outflowing gas can appear in projection, and demonstrate the potential for using velocity differences to observationally separate the two flows, provided sufficient kinematic resolution. They also show how differently the velocity components from inflowing and outflowing gas can appear in a velocity profile, highlighting that additional information (such as geometric context) is required to determine which velocity corresponds to which flow of gas.

To assess how well CGM kinematics can be studied observationally, Figure 11 builds on the bottom-right panel of Figure 10 by incorporating realistic kinematic resolution thresholds. Each panel shows the same map of pixel-by-pixel velocity differences between inflowing and outflowing gas, but now applies a resolution cut to simulate instrumental sensitivity. The color scale remains the same as in Figure 10, representing $|v_{in} - v_{out}|$. In these maps only pixels where the velocity difference exceeds a given threshold are colored; the rest are shown in gray. Colored pixels therefore indicate regions where an instrument with that kinematic resolution could re-

solve the kinematic separation between inflows and outflows.

The four panels represent different kinematic resolution limits: 300, 200, 100, and 30 km s⁻¹, shown from top-left to bottom-right. At the poorest resolution (300 km s⁻¹), very few regions meet the criterion for detectability. As the resolution improves to 200 km s⁻¹ more structure becomes apparent, especially near the central regions. At 100 km s⁻¹, significant portions of the halo show separable inflow and outflow signatures. By 30 km s⁻¹, much of the O VI-bright CGM becomes distinguishable, revealing widespread, spatially resolved kinematic differences between the two flow directions.

This analysis demonstrates that resolving the dynamics of CGM gas flows is only possible with high kinematic resolution. For much of the halo, a resolution finer than ~ 30 km s⁻¹ is required to capture the full range of O VI-emitting gas motions. These findings emphasize the need for next-generation spectrographs to combine both sensitivity to faint emission and fine velocity resolution to accurately trace CGM gas flows in emission.

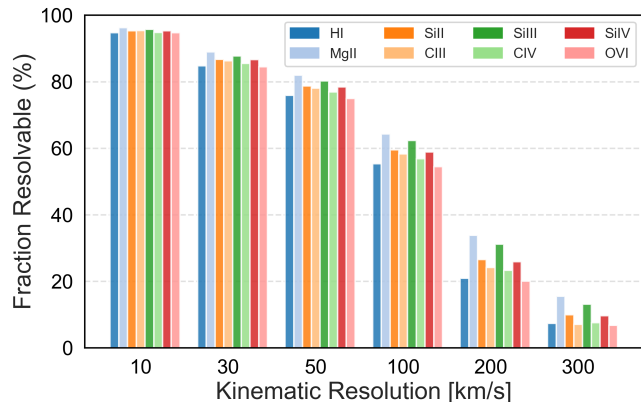


Figure 12. Fraction of projected area where inflows and outflows are kinematically distinguishable as a function of kinematic resolution for eight UV emission lines. Values represent the percentage of pixels from Figure 11 in which the absolute difference between inflow and outflow projected velocities exceeds the given kinematic resolution threshold. At low resolution (300 km s⁻¹), fewer than 20% of regions are distinguishable, while $\sim 60\%$ can be resolved at 100 km s⁻¹. A resolution of < 30 km s⁻¹ is required to distinguish inflow from outflow across more than 80% of the CGM area in all ions.

While Figs. 10 and 11 provide illustrative examples for O VI, Figure 12 extends this analysis to all eight ions to quantify the fraction of the projected CGM area that is kinematically resolvable as a function of instrumental resolution. We find that the resolvable fraction increases steeply with improving kinematic resolution. At 300 km

s⁻¹, less than 20% of the projected area of inflow/outflow overlap can be distinguished reliably. This fraction rises to $\sim 40\%$ at 200 km s⁻¹ and $\sim 60\%$ at 100 km s⁻¹. Achieving $\geq 80\%$ kinematic separation requires a resolution of 30 km s⁻¹ or better. While there are small variations between ions, all ions follow a similar trend. Note that the absolute values may vary depending on the halo or viewing angle. The trend itself is robust. Instruments aiming to constrain CGM kinematics should reach kinematic resolutions of ~ 30 km s⁻¹ or better to resolve the complexity of multiphase gas motions traced by UV emission lines.

Figure 13 illustrates the combined effects of spatial and kinematic resolution on the observability of CGM flows. Each row corresponds to a different spatial resolution (0.27, 1, 3, and 6 kpc). The left column shows maps of the absolute differences in emissivity-weighted line-of-sight velocities between inflowing and outflowing gas, as defined above. The color scale indicates the magnitude of the velocity difference (Δv), with gray regions denoting areas where the velocity difference falls below the threshold of 30 km s⁻¹. Colored regions represent areas that would be resolved at increasing levels of kinematic resolution.

The middle column shows surface brightness maps of O VI emission for the same spatial resolutions, identical in style to those in Figure 4. Colored pixels indicate regions with surface brightness above a sensitivity threshold of 100 photons s⁻¹ cm⁻² sr⁻¹. Gray regions fall below the sensitivity limit and are unresolved in terms of surface brightness.

The right column combines these two criteria — kinematic and spatial resolution — and shows the subset of pixels that are resolved in both velocity ($\Delta v > 30$ km s⁻¹) and surface brightness (SB > 100 photons s⁻¹ cm⁻² sr⁻¹). These maps represent the CGM gas that would be both detectable and kinematically distinguishable by an instrument with those capabilities. Pixels are color-coded by their Δv value, illustrating how changes in kinematic resolution would impact the observable fraction: for instance, only the yellow/orange pixels would remain resolved if the kinematic resolution were limited to 200 km s⁻¹.

This figure emphasizes that even if an instrument is sensitive enough to detect faint CGM emission, its kinematic resolution determines whether the dynamics of that gas can actually be measured. For example, at 0.27 kpc spatial resolution and a surface brightness threshold of 100 photons s⁻¹ cm⁻² sr⁻¹, an instrument with 30 km s⁻¹ spectral resolution would resolve over 90% of the detectable gas kinematically, while an instrument with

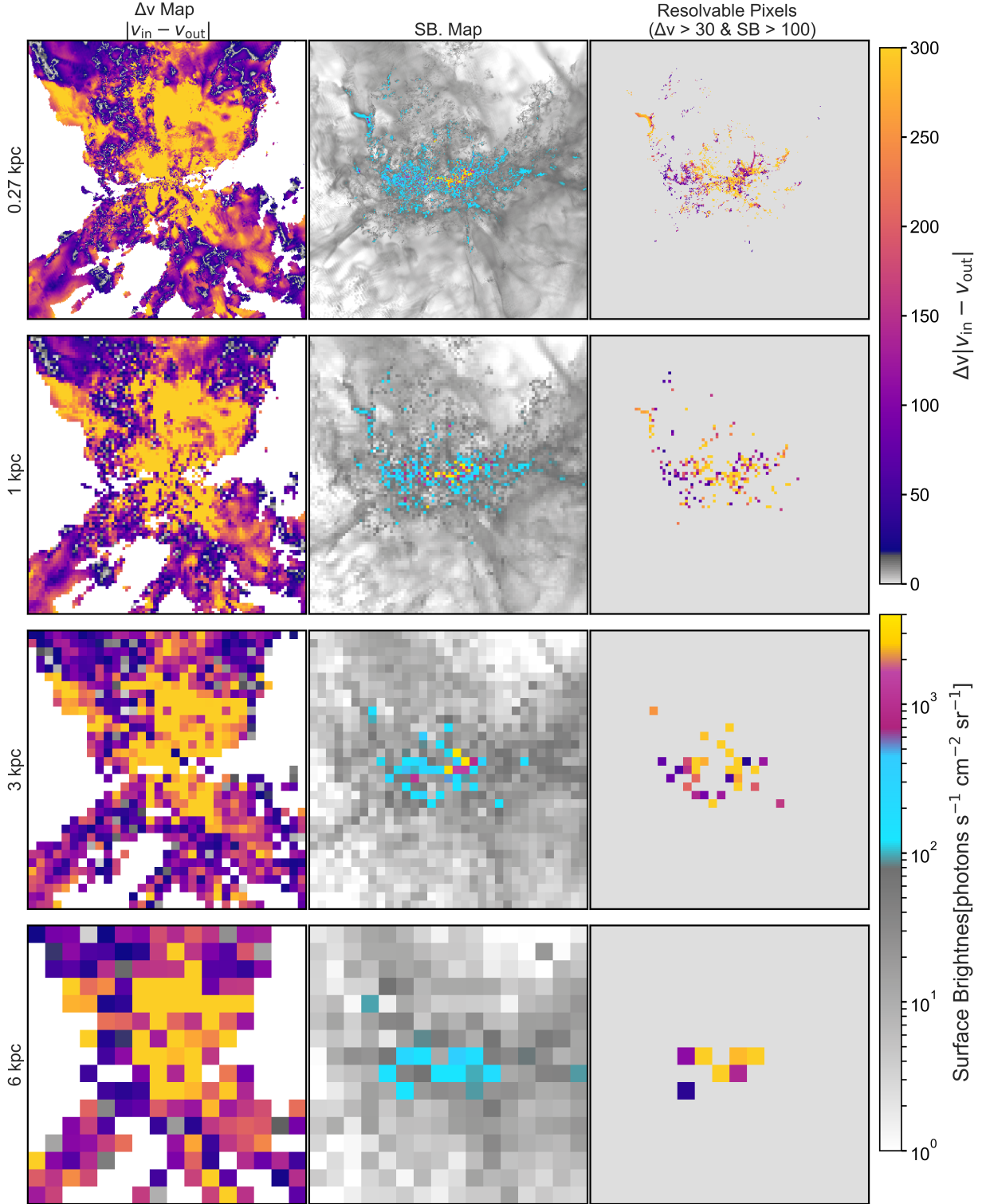


Figure 13. Combined effects of spectral and spatial resolution on CGM kinematic observability for the Maelstrom halo using O VI emission. Each row corresponds to a different spatial resolution (0.27, 1, 3, and 6 kpc, which correspond at $z = 0.5$ ($z = 0$) to ~ 0.04 (5.6), 0.16 (20), 0.5 (61), and 1 (120) arcsec, respectively). Left column: Maps of absolute projected velocity differences (Δv) between inflowing and outflowing gas (defined as $v_{\text{rad}} < -100 \text{ km s}^{-1}$ and $v_{\text{rad}} > 200 \text{ km s}^{-1}$, respectively). Gray pixels are unresolved ($\Delta v < 30 \text{ km s}^{-1}$); colored pixels indicate increasing Δv detectable at different kinematic resolutions: blue-purple ($30\text{--}100 \text{ km s}^{-1}$), purple-orange ($100\text{--}200 \text{ km s}^{-1}$), and orange-yellow ($>200 \text{ km s}^{-1}$). Middle column: Surface brightness maps showing detectable regions above a sensitivity threshold of $100 \text{ photons s}^{-1} \text{ cm}^{-2} \text{ sr}^{-1}$ (cyan, purple and yellow). Right column: Pixels that are resolved in both surface brightness and velocity (using $\Delta v = 30 \text{ km s}^{-1}$ and $\text{SB} = 100 \text{ photons s}^{-1} \text{ cm}^{-2} \text{ sr}^{-1}$ thresholds), color-coded by velocity difference. This panel shows how improved kinematic resolution enables separation of inflows and outflows in regions already observable in emission. At 30 km s^{-1} resolution, over 90% of the emission-resolved gas can be kinematically distinguished; at 200 km s^{-1} , this fraction drops to $\sim 40\text{--}50\%$.

only 200 km s^{-1} resolution would capture only about 40–50% of it.

6. CURRENT AND FUTURE EMISSION MAPPING INSTRUMENTS

Faint, extended emission poses strong challenges to our telescopes and instrumentation: at $1000 \text{ photons cm}^{-2} \text{ s}^{-1} \text{ sr}^{-1}$, for a source subtending 1 square arcsecond, a telescope of 8 meters in diameter will collect *one* source photon in 100 seconds of observation. Achieving a signal-to-noise ratio $\text{SNR} = 5$, with only Poisson shot noise accounted for, requires $2500 \text{ photons cm}^{-2} \text{ s}^{-1} \text{ sr}^{-1}$, larger spatial bins on the sky, a larger telescope, or a brighter source.

Simulations can assist with guiding requirements for instruments optimized for different kinds of observations. Simulations can also stimulate and inform the development of new instrument concepts by examining how physical outcomes depend on hypothetical instrument parameters. With detailed analysis of the FOGGIE simulations, we are able to quantify how sensitivity, wavelength coverage, and access to multiple ions recover the multiphase structure of the CGM in emission line maps. High spatial resolution (on the order of $\sim 1 \text{ kpc}$) enables detection of small-scale features, constraining the morphology and clumpiness of the gas. Sensitivity to low surface brightness ($\lesssim 500 \text{ photons cm}^{-2} \text{ s}^{-1} \text{ sr}^{-1}$) can reveal faint, extended structures and therefore recover a larger fraction of the ionized gas mass. Finally, kinematic resolution plays a critical role in completing our understanding of the CGM. While sensitivity determines whether CGM emission can be detected at all, kinematic resolution governs whether we can disentangle its dynamics. Distinguishing different velocity components, such as inflowing vs. outflowing gas, and recovering kinematics across ionization phases becomes increasingly feasible at kinematic resolutions of $\lesssim 30 \text{ km s}^{-1}$.

Building on these benchmarks, this section reviews a set of current and future instruments that have been or are intended to be applied to this problem. Figure 14 puts these instruments within this parameter space, using instrument properties listed in Table 3. We include two categories of instruments: those currently used or designed to study the CGM in the UV (top section), and those used to study CGM in $\text{H}\alpha$ (bottom section). For UV instruments, the surface brightness limits are shown for O VI emission, assuming exposure times of 10 and 100 hours. Note that some instruments appear in both sections of the table, as they are capable of observing both UV and $\text{H}\alpha$, depending on the redshift of the target.

The instruments already being used for CGM emission studies in Figure 14 and Table 3 are The Multi Unit Spectroscopic Explorer (MUSE, R. M. McDermid et al. 2008) the Keck Cosmic Web Imager Integral Field Spectrograph (KCWI, P. Morrissey et al. 2018), the Circumgalactic $\text{H}\alpha$ Spectrograph at the MDM Observatory (N. Melso et al. 2024), and the Dragonfly Telephoto Array (R. G. Abraham & P. G. van Dokkum 2014; D. Lokhorst et al. 2019b; S. Chen et al. 2024). Instruments operating in optical wavelength on large telescopes have the advantage of high spatial resolution and large collecting areas; conversely the suite of ions they can access in the rest frame (e.g., H I, O II) limits the temperature range of the gas they probe. The UV ions we focus on here are available at higher redshift and have been used to good effect with these powerful ground-based IFUs (e.g., D. C. Martin et al. 2019; H. Kusakabe et al. 2024; T. Ha et al. 2025).

It is perhaps surprising that for faint CGM emission, telescopes at the opposite end of the size scale can compete with 8-meter-class facilities on the ground. In space, the full range of diagnostic UV ions is available at $z < 1$, offering the largest practical set of physical diagnostics. Sky backgrounds are substantially darker in the UV than in the optical. And, for diffuse emission, spatial resolution adequate to resolve kiloparsec-scale structures can be achieved even by meter-scale telescopes. This region of the trade space has been pioneered by the Aspera SmallSat (H. Chung et al. 2021b), now in development, followed by proposed missions such as the Juniper CubeSat (E. M. Witt et al. 2025) and the MaGPIE Pioneer concept (D. Vorobiev 2025). Further down the road there is the prospect for future flagship concepts like the Habitable Worlds Observatory (HWO), which apply extreme sensitivity at fine spatial resolution.

Figure 14 presents a set of 2D comparisons for individual characteristics and a 3D plot that brings together all of the critical parameters discussed above. To maintain clarity and focus, we include only instruments capable of observing the CGM in the UV. The parameters shown in this figure are listed in Table 3 (top section). In the 2D plots, for consistency, the x-axis shows the O VI surface brightness sensitivity (in $\text{photons cm}^{-2} \text{ s}^{-1} \text{ sr}^{-1}$) for each instrument, as listed in the last two columns of Table 3. Error bars indicate the range of surface brightness limits corresponding to exposure times of $T_{\text{exp}} = 10$ and 100 hours, while the marker denotes the mean value.

The first panel plots spatial resolution on the y-axis, converted from angular resolution to physical kpc by assuming the lowest redshift targets for each instrument (see the fifth column of Table 3). The second panel shows the spectral resolution of each instrument in km

Table 3. Instrumental parameters for CGM Emission

Instrument	z Range	FOV	Spatial Resolution		Spectral Resolution		Wavelength Range Å	SB Limits ^b	
			arcsec	kpc ^a	R –	Δv km s ⁻¹		10 hr ph cm ⁻²	100 hr s ⁻¹ sr ⁻¹
UV / Optical Instruments					O VI				
MUSE	> 2	1' × 1'	0.2	1.7	1770–3590	80–170	4650–9300	778	246
KCWI	> 2	20'' × 8–33'	0.4	3.5	1000–20000	15–300	3500–10500	2795	884
HWO	< 1	2' × 2'	0.05	0.001	15000	20	900–3000	320	100
Aspera	< 0.01	1° × 30''	30	0.64	1500	200	1030–1040	3123	987
Juniper	< 0.024	30'' × 30''	20	0.43	7500–13000	23–40	1025–1929	2256	713
MaGPIE	< 0.02	5' × 12'	30	0.64	1500	200	1000–3000	1354	428
H α / Optical Instruments					H α				
MUSE	< 0.42	1' × 1'	0.2	1.7	1770–3590	80–170	4650–9300	778	246
KCWI	< 0.60	20'' × 8–33'	0.4	3.5	1000–20000	15–300	3500–10000	2795	884
CH α S	< 0.01	10' × 10'	1.3	0.03	10000–20000	15–30	4000–9000	1580	475
Dragonfly	< 0.2	2.6° × 1.9°	2.8	0.06	750	400	5007–6563	2500	1000

^aSpatial resolutions in kpc are computed at the lowest redshift in the listed z range (or at $z=0.001$ if the minimum is 0)

^bThe reported limits are for observed line fluxes; the intrinsic limits are higher by a factor of $(1+z)$.

NOTE—Sources: MUSE (<https://www.eso.org/sci/facilities/develop/instruments/muse.html>), KCWI (<https://www2.keck.hawaii.edu/inst/kcwi/primer.html>), CH α S (N. Melso et al. 2022), HWO (The LUVUOIR Team 2019), Aspera (H. Chung et al. 2021c), Juniper (E. M. Witt et al. 2025), MaGPIE (D. Vorobiev 2025), Dragonfly (D. Lokhorst et al. 2019b).

s⁻¹ (resolving power ranges are provided in the sixth column of Table 3). The third panel plots the wavelength coverage on the y-axis, which serves as a proxy for how well each instrument can capture the multiphase structure and mass budget of the CGM. The final panel combines these parameters into a single 3D view: spatial resolution, spectral resolution, and sensitivity are placed along the three axes, while wavelength coverage is encoded in the marker size (larger symbols correspond to broader wavelength ranges). In all panels, current instruments are represented with star symbols and upcoming/future missions with circles. Gray shaded regions in the 2D panels, and a gray box in the 3D panel, indicate the parameter space identified in this study as critical for detecting faint, multiphase CGM emission and for resolving its underlying kinematics.

Starting with the first 2D panel, the gray shaded region on the right marks the sensitivity required to detect faint, extended CGM emission. For consistency, the values shown are calculated for O VI (the common ion being pursued by all instruments) and for exposure times of 10 and 100 hours. Among current facilities, MUSE reaches into the shaded region, demonstrating its capability to probe the faint end of CGM emission, whereas KCWI remains well outside this regime under the same assumptions. Among the upcoming missions, HWO is the only instrument that robustly meets the shaded sen-

sitivity range, while MaGPIE approaches this threshold for sufficiently long integrations.

The shaded region at the top of the panel indicates the ideal spatial resolution, $\lesssim 1$ kpc, needed to resolve small-scale structures and to detect the morphology and clumpiness of the CGM. Current instruments such as MUSE and KCWI fall short of this threshold, largely because their design makes them suitable for mainly detecting UV rest-frame emission at higher redshifts. Even when using their narrowest image slices, the spatial resolution is a few kpc for targets at $z \gtrsim 2$. On the other hand, upcoming missions are expected to provide substantial improvements: three of four future facilities shown in the figure fall within the shaded region for spatial resolution. The small satellites (Aspera, Juniper) are designed to observe low-redshift galaxies, where smaller slicers and nearby targets make sub-kpc physical resolution possible. HWO, meanwhile, stands out for its ability to maintain high spatial resolution even at higher redshifts, with fine spatial sampling that ensures small-scale CGM features remain accessible.

The second panel shows kinematic resolution on the y-axis, with the gray shaded region (< 30 km s⁻¹) marking the ideal regime for studying CGM kinematics. Each instrument is plotted at its average spectral resolution across the full operating range, with error bars indicating the span of values (see Table 3). Among current

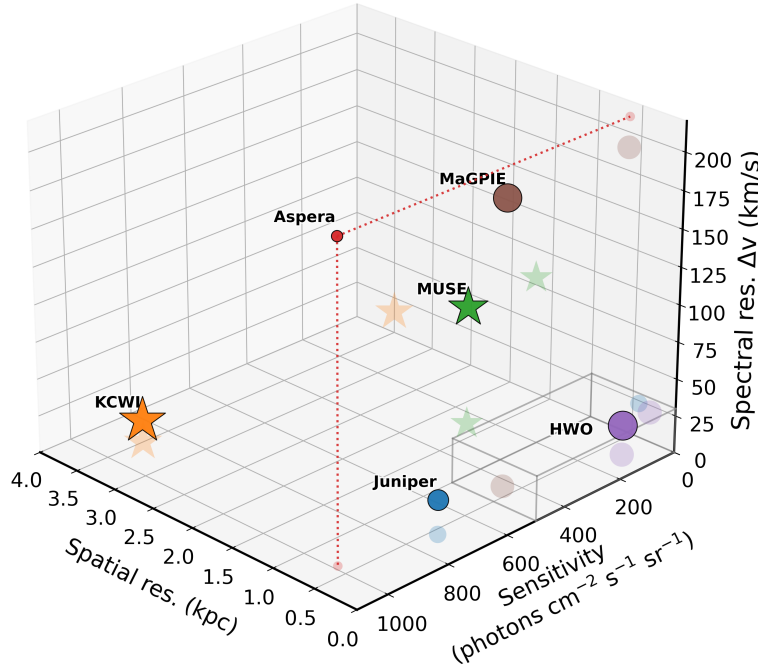
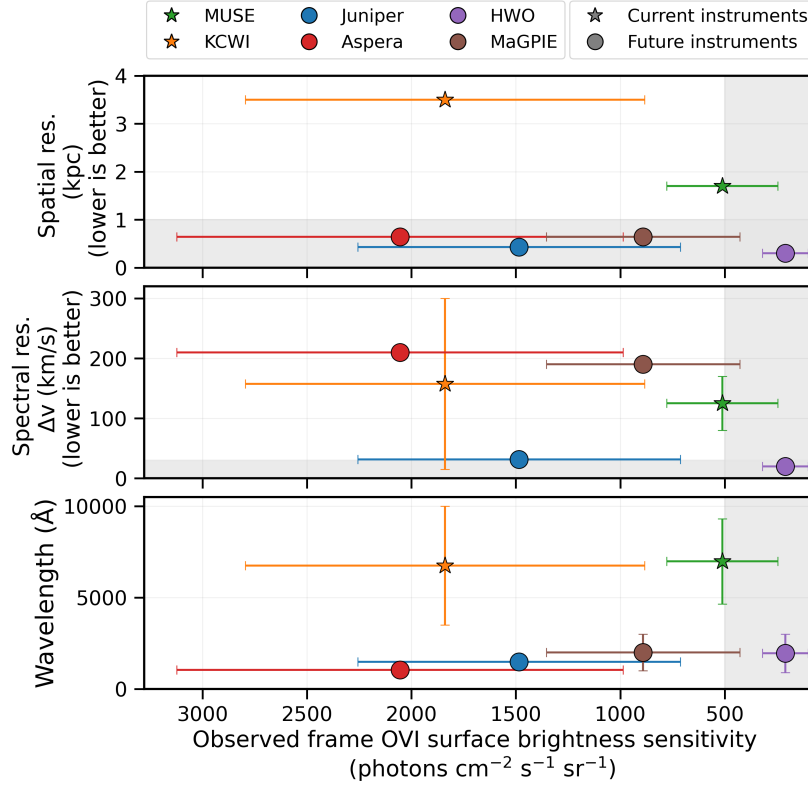


Figure 14. Comparison of current (stars) and future (circles) instruments designed/suitable for CGM studies in emission across multiple performance planes. Sensitivity (photons s⁻¹ cm⁻² sr⁻¹) is shown on the x-axis of the three 2D panels. First panel: Spatial resolution versus sensitivity highlights mapping capability. Second panel: kinematic resolution versus sensitivity illustrates kinematic resolving power. Third panel: Wavelength range versus sensitivity shows multiphase detection capability. Grey shaded regions mark regimes of particularly strong performance (sensitivity $\lesssim 500$ photons s⁻¹ cm⁻² sr⁻¹ combined with spatial resolution < 1 kpc, kinematic resolution < 30 km s⁻¹). Last panel: A 3D view combines all three axes, spatial resolution, sensitivity, and kinematic resolution, with marker size proportional to the covered wavelength range, providing a holistic comparison of current and future instruments. The gray box corresponds to the shaded regions in the 2D panels. These performance thresholds serve as a guide for the design of next-generation instruments.

facilities, KCWI reaches into the shaded region at its highest resolving power, while MUSE, with a spectral resolution of $\sim 100 \text{ km s}^{-1}$, falls short. However, this performance is not prohibitive: for example, Figure 12 shows that with $\sim 100 \text{ km s}^{-1}$ resolution, $\sim 60\%$ of the field of view can still be kinematically resolved. Among UV missions, the Juniper CubeSat stands out for its spectral resolution and coverage of multiple ions, enabling the recovery of CGM kinematics at low redshift. HWO will likewise achieve the precision required to resolve velocity components across multiple phases. Aspera and MaGPIE, by contrast, are not as optimized for kinematic studies.

The third 2D panel shows the wavelength range covered by each instrument. Broader coverage allows an instrument to probe a wider set of CGM phases and to recover the total CGM mass more accurately. Among current facilities, MUSE spans a larger wavelength range than KCWI, giving it stronger leverage on detecting multiphase structure. Looking ahead, HWO stands out with the broadest coverage, enabling access to the largest suite of diagnostic ions. Juniper and MaGPIE have comparable wavelength ranges, each designed to target a subset of key ions spanning both low- and high-ionization states. This focused coverage still provides valuable insights into the multiphase CGM, even if the overall range is less complete. Aspera is intentionally designed to observe only O VI.

Finally, the 3D panel places each instrument in a parameter space defined by spatial resolution, spectral resolution, and sensitivity, using the best available values from Table 3. Marker size corresponds to the wavelength range covered by each instrument. For clarity, each marker is mirrored as a shadow onto the spatial-sensitivity and sensitivity-spectral resolution planes, with a dotted guide line for Aspera to aid the reader's eye. This visualization highlights where current instruments sit relative to the critical parameter space identified in this study, and how future facilities are expected to advance. Markers lying closer to the gray box indicate better overall performance. Among current instruments, MUSE performs reasonably well in spatial resolution and sensitivity, enabling the detection of CGM emission, but falls short in spectral resolution. KCWI, in contrast, achieves a high spectral resolution suitable for kinematic studies, but its lower sensitivity limits its ability to detect faint emission. Looking forward, future missions must improve simultaneously across all of these parameters. CubeSats such as Juniper demonstrate promising advances in spectral resolution at low cost, providing valuable insight into the CGM of nearby galaxies. However, probing larger sam-

ples across a broad redshift range will require instruments that combine high performance in all dimensions. Achieving the full set of ideal requirements in a single facility is challenging, which is why space observatories like HWO are so critical: by approaching the optimal regime across spatial, spectral, and sensitivity domains, they promise to revolutionize our understanding of the CGM and its role in galaxy evolution.

This analysis also suggests that optical and UV instruments can combine to observe the same targets in the nearby universe, complementing one another and collecting a set of ionization diagnostics that spans the full available range. For low redshift, optical telescopes will be observing rest-frame optical lines (e.g., $\text{H}\alpha$, $[\text{O II}]$). While their sizes and therefore angular resolution are quite different, their surface brightness limits and the exposure times needed to reach these limits are similar (Table 3). One particular use case would be to focus the smaller spatial resolution elements of large telescopes on interesting regions discovered in the CGM of a nearby galaxy, zooming in on small structures and examining their ionization and kinematics in detail. With current and future instrumentation in both space (Aspera, Juniper, HWO) and on the ground (e.g. E-ELT/HARMONI), there are excellent prospects for addressing CGM physics from multiple complementary instruments.

7. SUMMARY AND CONCLUSIONS

Observing the CGM in emission provides a powerful means of accessing the spatial and kinematic structure of gas that regulates galactic accretion and feedback. We have examined the detectability and kinematic separability of eight UV emission lines using the high-resolution FOGGIE simulations. Our key findings are:

- A wide range of emission lines is essential to capture the multiphase structure of the CGM. High-ionization lines like O VI trace more diffuse emission from gas at $T \gtrsim 10^5 \text{ K}$, while low-ion lines like $\text{H}\alpha$, Si II, and Mg II trace clumpier, denser structures. Intermediate ions (e.g., C IV, Si IV, C III, Si III) recover elements of both regimes. Observations restricted to one ion or a small set will miss structures traced by other ions, and multi-line observations are required to build a comprehensive picture of the multiphase CGM.
- Surface brightness sensitivity at $500 \text{ photons cm}^{-2} \text{ s}^{-1} \text{ sr}^{-1}$ or below is the primary requirement for revealing the full mass and spatial extent of CGM emission. As surface brightness limits rise above this threshold, the fraction of detectable gas drops

sharply, especially for higher ionization lines like O VI and C IV (Figure 6). In contrast, low ions such as H α and Mg II retain higher observable mass fractions at moderate sensitivity owing to a greater degree of clumping. These trends underscore the need for future instrumentation, especially in the UV, to prioritize sensitivity below 500 photons cm⁻² s⁻¹ sr⁻¹ to uncover the faint, extended components of the CGM.

- Resolving CGM structures at the \sim kpc scale is essential for mapping morphology and structures in the CGM. With coarser resolution ($\geq 3 - 6$ kpc), faint CGM features such as accreting filaments and cold clumps are smoothed out, even if their total flux (and mass) remains detectable. Figure 4 shows small-scale features are preserved at 1 kpc resolution but begin to blur or vanish at lower resolution.
- Good kinematic resolution ($\Delta v \lesssim 30$ km s⁻¹) is required to relate, or to distinguish, different phases of the gas when seen in projection. Typical velocity offsets between widely separated ion pairs, e.g., H I and O VI, are only resolvable at kinematic resolutions finer than ~ 30 km s⁻¹, and largely disappear at coarser resolution. In contrast, low-ionization species like Mg II show velocity structures closely aligned with H I, and their kinematics remain indistinguishable even at 30 km s⁻¹ resolution. This highlights how kinematic resolution enables separation of multiphase gas motions in the CGM.
- Distinguishing inflowing from outflowing gas also requires good kinematic resolution. Across all ions, the fraction of CGM area where inflow and outflow can be kinematically separated increases from $\leq 20\%$ at 300 km s⁻¹ to $\geq 90\%$ at 30 km s⁻¹. These results demonstrate that recovering the full dynamical picture of the CGM—including its multiphase structure and circulation patterns—requires spectrographs capable of achieving $\Delta v \leq 30$ km s⁻¹.

The landscape of instrumentation intended to detect CGM emission is evolving rapidly. Our comparison of current and proposed UV/optical facilities (Figure 14) shows that no single current instrument is optimized for depth, spatial and kinematic resolution, and coverage of multiphase ions. Given the practical limitations of instrument design, it is likely that no instrument will optimize on all three axes at once; our simulations therefore offer quantitative guidance about the trade-space

along these three axes. For example, if kinematic resolution cannot be achieved at the desired level, designers should seek to cover a broad set of ions at good spatial resolution. Where covering multiple ions is not possible, deep surface brightness limits could be pursued with good spatial and/or kinematic resolution. The parameter space in Figure 14 will likely continue to be populated by new and innovative instrument concepts developed to address this important problem. In this time of growth, our simulations also offer a quantitative basis for making tradeoffs and comparisons between instruments, and for computing how instruments with different optimizations can operate together in a complementary fashion to reveal the complex flows of the CGM in detail.

ACKNOWLEDGMENTS

We thank J. C. Howk for insightful discussion and suggestions. VS was supported for this work in part by NASA via an Astrophysics Theory Program grant #80NSSC24K0772, HST AR #17549, and HST GO #17093. CWT was supported for this work in part by NASA via a Theoretical and Computational Astrophysics Networks grant #80NSSC21K1053 and JWST AR #5486. VS and CWT were also supported by HST AR #16151. BWO acknowledges support from NSF grants #1908109 and #2106575, NASA ATP grants 80NSSC18K1105 and 80NSSC24K0772, and NASA TCAN grant 80NSSC21K1053. CL was supported by NASA through the NASA Hubble Fellowship grant #HST-HF2-51538.001-A awarded by the Space Telescope Science Institute, which is operated by the Association of Universities for Research in Astronomy, Inc., for NASA, under contract NAS5-26555. AA acknowledges support from the INAF Large Grant 2022 “Extragalactic Surveys with JWST” (PI Pentericci) and from the European Union – NextGenerationEU RFF M4C2 1.1 PRIN 2022 project 2022ZSL4BL INSIGHT. RA acknowledges funding from the European Research Council (ERC) under the European Union’s Horizon 2020 research and innovation programme (grant agreement 101020943, SPECMAP-CGM).

Computations described in this work were performed using the publicly-available ENZO code (<http://enzo-project.org>), which is the product of a collaborative effort of many independent scientists from numerous institutions around the world. Their commitment to open science has helped make this work possible. The python packages MATPLOTLIB (J. D. Hunter 2007), NUMPY (S. v. d. Walt et al. 2011), ROCKSTAR (P. S. Behroozi et al. 2013), TANGOS (A. Pontzen & M. Tremmel 2018),

SCIPY (P. Virtanen et al. 2020), YT (M. J. Turk et al. 2011), and ASTROPY (Astropy Collaboration et al. 2022) were all used in parts of this analysis or in products used by this paper. Resources supporting this work were provided by the NASA High-End Computing (HEC) Program through the NASA Advanced Supercomputing (NAS) Division at Ames Research Center and were sponsored by NASA’s Science Mission Directorate.

AUTHOR CONTRIBUTIONS

VS led the analysis and writing of the paper. JT provided scientific guidance, refined the interpretation by suggesting additional diagnostics, and contributed to the writing. MSP, BWO, and JT are the principal investigators of the FOGGIE collaboration; they obtained funding for, developed, and ran the simulations used in

this work. MSP and BWO also provided valuable feedback and insights throughout the discussion. CL contributed to the interpretation of the results and shared her experience with similar analyses. LC developed the pipeline for obtaining emissivities from Cloudy tables and provided additional insights based on related analyses. CWT developed the code used to remove the H I disk and provided feedback on the draft. BDS wrote the CIAOLoop code that was essential for generating the Cloudy tables and developed the initial conditions for the FOGGIE simulations. JKW contributed through discussions and constructive feedback. AA, RA, AJF, NL, and ACW provided insights through discussions during the analysis phase, as well as feedback on the final draft.

APPENDIX

A. SURFACE BRIGHTNESS UNITS AND EQUIVALENCIES

Surface brightness of extended source emission is expressed in a variety of units without consistent usage in the existing literature. For line emission, the most common units are $\text{erg s}^{-1} \text{cm}^{-2} \text{arcsec}^{-2}$ and $\text{photons s}^{-1} \text{cm}^{-2} \text{sr}^{-1}$. The former are convenient when dealing with data or instruments with spatial resolution elements on the order of arcseconds. The later, sometimes known as “line units” or “LU”, result in quantities of order 100-10000 and can be compared without knowing the identity of the underlying line. The conversion between the two units requires knowing the *observed* wavelength of a given emission line.

These two conversions are as follows. For a line observed at wavelength λ_0 , the photon energy $E_{ph} = hc/\lambda_0$, where h is Planck’s constant (Planck Collaboration et al. 2016) and c is the speed of light. Thus

$$f_{LU} = f_{\lambda} \times (1 \text{ photon}/E_{ph}) \times (4.25 \times 10^{10} \text{ arcsec}^2 \text{ sr}^{-1}), \quad (\text{A1})$$

where f_{LU} then has units of $\text{photons s}^{-1} \text{cm}^{-2} \text{sr}^{-1}$.

Here are some worked examples for concreteness. For O VI observed at the rest frame, $\lambda_0 = 1032 \text{ \AA}$. We can express the speed of light as $c = 2.9979 \times 10^{18} \text{ \AA s}^{-1}$. Each detected photon has energy hc/λ_0 or $E_{ph} = 1.93 \times 10^{-11} \text{ erg}$. By Equation A1,

$$f_{LU}^{OVI} = 2.21 \times 10^{21} f_{\lambda}^{OVI} \quad (\text{A2})$$

M. Hayes et al. (2016) reported O VI detections at $f_{\lambda} = 10^{-17} \text{ erg s}^{-1} \text{cm}^{-2} \text{arcsec}^{-2}$. According to Equation A2, this value converts to $22064 \text{ photons s}^{-1} \text{cm}^{-2} \text{sr}^{-1}$. Going in the other direction, B. Otte et al. (2003) reported an O VI detection in NGC 4631 at $f_{LU} = 8000 \text{ photons s}^{-1} \text{cm}^{-2} \text{sr}^{-1}$. This converts to $f_{\lambda} = 3.63 \times 10^{-17} \text{ erg s}^{-1} \text{cm}^{-2} \text{arcsec}^{-2}$. For lines that are observed with some redshift, care must be taken to apply the correct $(1+z)$ factor to the photon energy. For a general rule of thumb, a reasonable approximation is that 200 LU converts to $10^{-19} \text{ erg s}^{-1} \text{cm}^{-2} \text{arcsec}^{-2}$ for O VI and $6 \times 10^{-20} \text{ erg s}^{-1} \text{cm}^{-2} \text{arcsec}^{-2}$ for C IV.

For our assumed Λ CDM cosmology, 1 arcsecond subtends a physical size of 8.54 kpc at $z = 2$, and 0.21 kpc at $z = 0.01$ (about $d = 40 \text{ Mpc}$). These two regimes correspond to redshifted UV lines observed at sub-arcsecond spatial resolution, and rest-frame UV lines observed at $\sim 20 \text{ arcsec}$ resolution. These two very disparate extremes of telescope size and spatial resolution both yield physical resolutions near $\sim 1 \text{ kpc}$ (Figure 3).

B. CGM MASS FRACTION MAPS FOR ALL IONS

For completeness, we include here the full set of heatmaps analogous to Figure 5, showing the observable CGM mass fractions for all eight emission lines analyzed in this study. Figure 15 presents the results for edge-on galaxy projections,

while Figure 16 shows the corresponding face-on projections. These results reinforce the conclusion discussed in the main text: sensitivity has a more significant impact than spatial resolution on the ability to recover CGM mass across different ions.

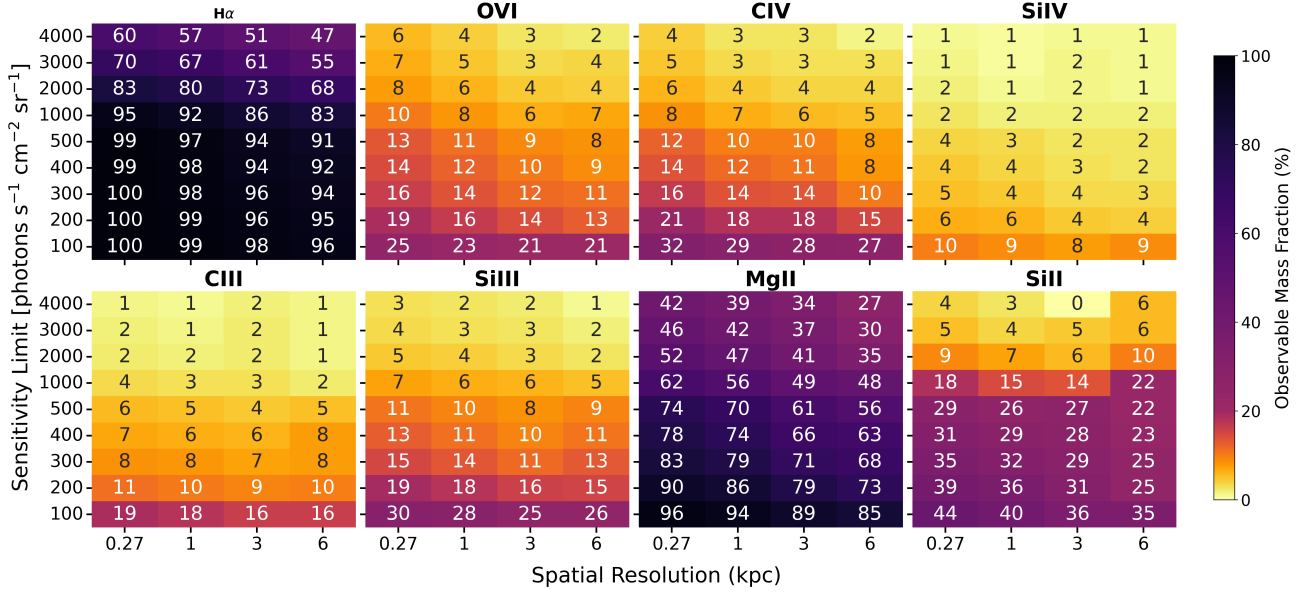


Figure 15. Observable CGM mass fraction as a function of spatial resolution (x-axis) and surface brightness sensitivity (y-axis), for eight emission lines, averaged over six FOGGIE halos, edge-on. Each cell shows the percentage of total CGM mass detectable above the given sensitivity limit at the specified resolution, with values color-coded and overlaid. As expected, observability decreases with lower sensitivity and coarser resolution, though sensitivity plays a stronger role: at fixed resolution, increasing the detection threshold from 100 to 500 reduces the detectable mass by more than 50% in several ions. These results emphasize that achieving high sensitivity is critical for maximizing CGM detection, particularly for tracing diffuse, highly ionized gas.

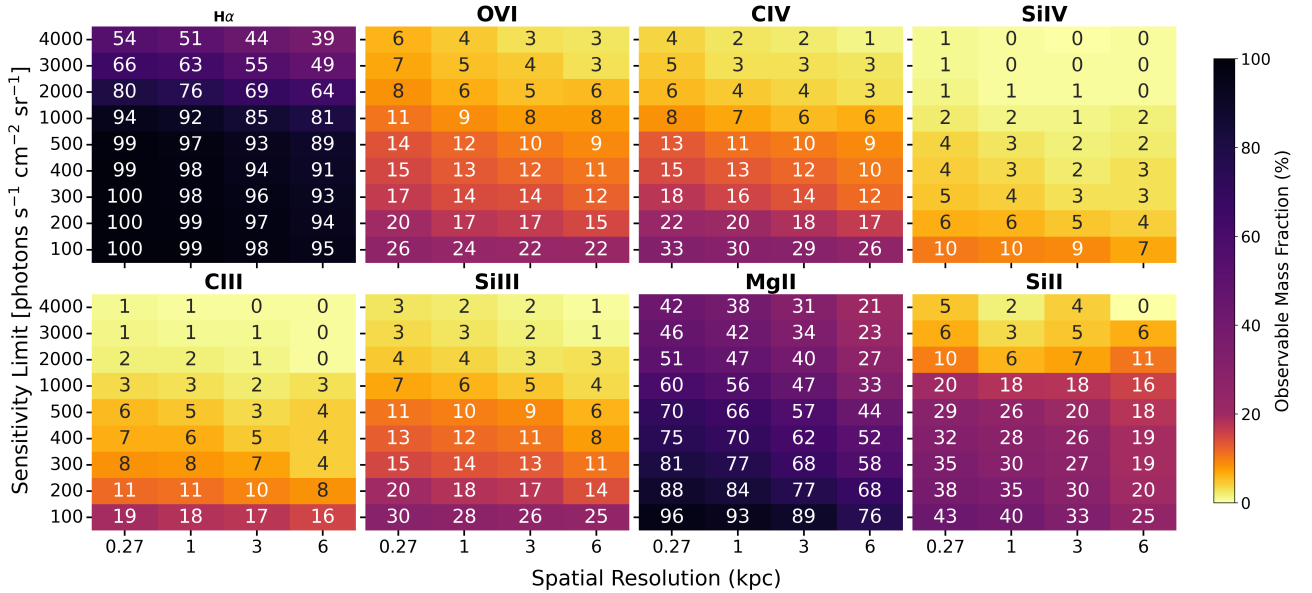


Figure 16. Same as Figure 5 but for a face-on view.

C. CONSTRUCTING CLOUDY EMISSIVITY TABLES

To generate the emissivity tables used in this work, we followed the pipeline described in [L. Corlies et al. \(2020\)](#) and implemented using the CIAOLOOP package (https://github.com/brittonsmith/cloudy_cooling_tools.git). Below, we provide the key commands from the parameter file used to run CIAOLOOP and produce the emissivity grids, along with a brief explanation of the output units and how they are converted to the values used in our analysis. [Figure 17](#) shows 2D histograms of temperature versus number density for each ion, color-coded by emissivity; these plots highlight the physical conditions under which each ion emits most strongly.

C.0.1. *Example Parameter File*

The following configuration was used in addition to the standard run commands specifying the paths to CLOUDY and output directories.

```
##### Line Map Parameters #####

# Minimum and maximum temperatures (K)
coolingMapTmin = 1e3
coolingMapTmax = 1e8

# Number of temperature steps (log-spaced)
coolingMapTpoints = 51

coolingMapUseJeansLength = 1

# Emission lines to save

lineMapLine = H 1 6563
lineMapLine = Mg 2 2796
lineMapLine = Si 2 1260
lineMapLine = C 3 1910
lineMapLine = Si 3 1207
lineMapLine = C 4 1548
lineMapLine = Si 4 1394
lineMapLine = O 6 1032
lineMapLine = O 6 1038
#####
##### Commands executed for each run #####

command failures 200 times map
command iterate to convergence max=2 error=0.20
command CMB redshift 0.00
command Table HM12 redshift 0.00
command set WeakHeatCool -20
command no H2 molecule
command no charge transfer
#####
##### Parameters looped over #####

# Loop over hydrogen number density (cm^-3)
loop [hden] (-6;2;0.5)
command metals 0 log
```

This configuration assumes a UV background from [F. Haardt & P. Madau \(2012\)](#) (HM12) at $z = 0$, solar metallicity (which is then scaled linearly by each cell's metallicity during post-processing), temperature and density ranges as described in [Section 2.3](#), and the set of emission lines analyzed in this paper (see [Table 2](#)).

C.0.2. *Emissivity Units and Conversion*

CLOUDY outputs emissivities as $\text{emissivity}/n_{\text{H}}^2$ in units of $\text{erg cm}^3 \text{ s}^{-1}$. To obtain the final surface brightness, we first multiply the tabulated emissivity values by n_{H}^2 to recover the total emissivity. We then scale this by the metallicity of each simulation cell, and convert the result from energy to photon units using the method described in [Appendix A](#). Finally, we use Υ_{T} ([M. J. Turk et al. 2011](#)) to project along the line of sight, integrating over the simulation cell depth Δl (in cm) to compute the surface brightness in $\text{photons cm}^{-2} \text{ s}^{-1} \text{ sr}^{-1}$.

C.0.3. Emissivity as a function of temperature and number density

Figure 17 shows temperature–number density phase plots for the Maelstrom halo, color-coded by the emissivity of each ion. The emissivity values are calculated as described in Sections 2.3, C.0.1, and C.0.2. Dark blue pixels indicate regions of parameter space where gas exists but does not emit significantly in the corresponding ion shown in each subplot.

These plots illustrate the thermodynamic conditions under which each ion emits most strongly. High-ionization lines like O VI exhibit peak emissivity at high temperatures ($T \sim 10^{5.5}–10^6$ K) and low densities, reflecting their origin in hot, diffuse CGM gas. In contrast, low-ionization species such as Mg II and Si II peak at cooler temperatures ($T \sim 10^4$ K) and higher densities, typically associated with denser clumps and filaments. Other ions (e.g., C III, Si III) trace a broader range of densities and temperatures, highlighting their role in bridging different phases of the CGM. These emissivity distributions motivate the use of multiple emission lines to map the full structure of the CGM.

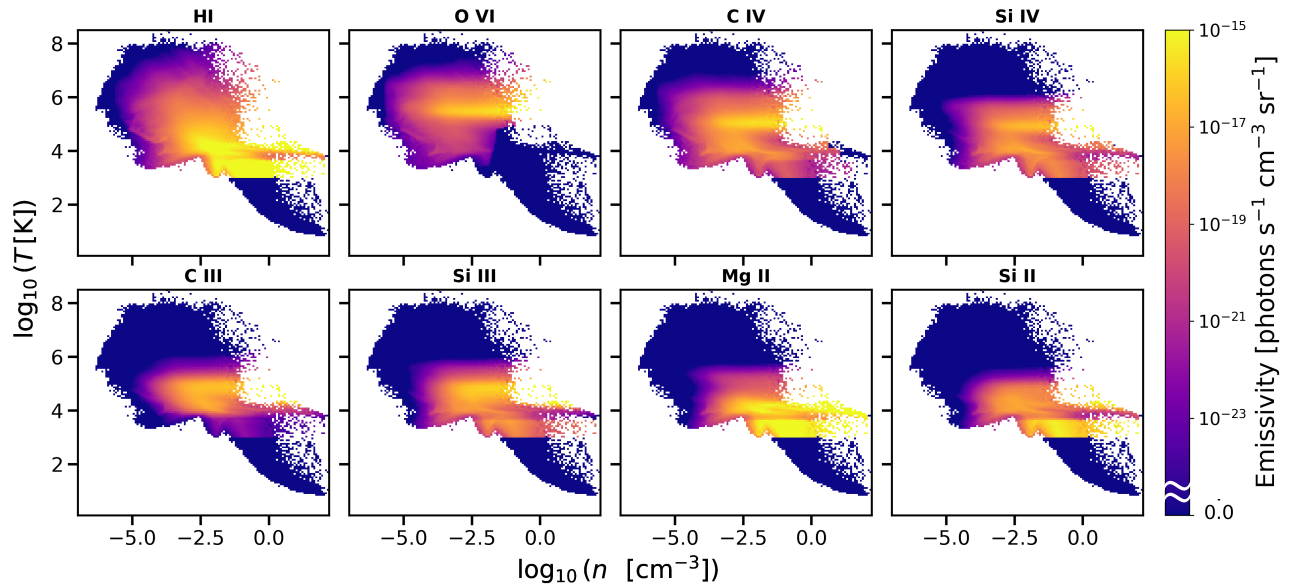


Figure 17. 2D histograms showing the emissivity distribution of each ion as a function of gas temperature and number density for the Maelstrom halo at $z = 0.5$. The dark blue background indicates all gas, while the colored pixels highlight regions where emission from that ion is present. The sharp cutoff at $\log_{10} T = 3$ arises because the minimum temperature included in the CLOUDY emissivity tables is $\log_{10} T = 3$, as this is the minimum temperature we expect to find in the CGM and we do not focus on ISM emission in this work.

REFERENCES

- Abraham, R. G., & van Dokkum, P. G. 2014, *PASP*, 126, 55, doi: [10.1086/674875](https://doi.org/10.1086/674875)
- Acharyya, A., Peeples, M. S., Tumlinson, J., et al. 2024, arXiv e-prints, arXiv:2404.06613, doi: [10.48550/arXiv.2404.06613](https://doi.org/10.48550/arXiv.2404.06613)
- Astropy Collaboration, Price-Whelan, A. M., Lim, P. L., et al. 2022, *ApJ*, 935, 167, doi: [10.3847/1538-4357/ac7c74](https://doi.org/10.3847/1538-4357/ac7c74)
- Augustin, R., Péroux, C., Hamanowicz, A., et al. 2021, *MNRAS*, 505, 6195, doi: [10.1093/mnras/stab1673](https://doi.org/10.1093/mnras/stab1673)
- Augustin, R., Quiret, S., Milliard, B., et al. 2019, *MNRAS*, 489, 2417, doi: [10.1093/mnras/stz2238](https://doi.org/10.1093/mnras/stz2238)
- Augustin, R., Tumlinson, J., Peeples, M. S., et al. 2025, arXiv e-prints, arXiv:2501.06551, doi: [10.48550/arXiv.2501.06551](https://doi.org/10.48550/arXiv.2501.06551)
- Bahcall, J. N., & Spitzer, Jr., L. 1969, *ApJL*, 156, L63, doi: [10.1086/180350](https://doi.org/10.1086/180350)
- Behroozi, P. S., Wechsler, R. H., & Wu, H.-Y. 2013, *ApJ*, 762, 109, doi: [10.1088/0004-637X/762/2/109](https://doi.org/10.1088/0004-637X/762/2/109)
- Bertone, S., Schaye, J., Booth, C. M., et al. 2010, *MNRAS*, 408, 1120, doi: [10.1111/j.1365-2966.2010.17188.x](https://doi.org/10.1111/j.1365-2966.2010.17188.x)

- Bordoloi, R., Lilly, S. J., Kacprzak, G. G., & Churchill, C. W. 2014, *ApJ*, 784, 108, doi: [10.1088/0004-637X/784/2/108](https://doi.org/10.1088/0004-637X/784/2/108)
- Bordoloi, R., O'Meara, J. M., Sharon, K., et al. 2022, *Nature*, 606, 59, doi: [10.1038/s41586-022-04616-1](https://doi.org/10.1038/s41586-022-04616-1)
- Borthakur, S., Heckman, T., Tumlinson, J., et al. 2016, *ApJ*, 833, 259, doi: [10.3847/1538-4357/833/2/259](https://doi.org/10.3847/1538-4357/833/2/259)
- Bowen, D. V., Chelouche, D., Jenkins, E. B., et al. 2016, *ApJ*, 826, 50, doi: [10.3847/0004-637X/826/1/50](https://doi.org/10.3847/0004-637X/826/1/50)
- Brummel-Smith, C., Bryan, G., Butsky, I., et al. 2019, *The Journal of Open Source Software*, 4, 1636, doi: [10.21105/joss.01636](https://doi.org/10.21105/joss.01636)
- Bryan, G. L., Norman, M. L., O'Shea, B. W., et al. 2014, *ApJS*, 211, 19, doi: [10.1088/0067-0049/211/2/19](https://doi.org/10.1088/0067-0049/211/2/19)
- Cadiou, C., Katz, H., Rey, M. P., et al. 2025, arXiv e-prints, arXiv:2510.05667. <https://arxiv.org/abs/2510.05667>
- Cen, R., & Ostriker, J. P. 2006, *ApJ*, 650, 560, doi: [10.1086/506505](https://doi.org/10.1086/506505)
- Chatzikos, M., Bianchi, S., Camilloni, F., et al. 2023, *RMxAA*, 59, 327, doi: [10.22201/ia.01851101p.2023.59.02.12](https://doi.org/10.22201/ia.01851101p.2023.59.02.12)
- Chen, S., Lokhorst, D. M., Pasha, I., et al. 2024, in *Society of Photo-Optical Instrumentation Engineers (SPIE) Conference Series*, Vol. 13094, Ground-based and Airborne Telescopes X, ed. H. K. Marshall, J. Spyromilio, & T. Usuda, 130942J, doi: [10.1117/12.3019491](https://doi.org/10.1117/12.3019491)
- Chen, S., Lokhorst, D. M., Pasha, I., et al. 2025, *PASP*, 137, 084103, doi: [10.1088/1538-3873/adedb8](https://doi.org/10.1088/1538-3873/adedb8)
- Chung, H., Vargas, C. J., & Hamden, E. 2021a, *ApJ*, 916, 7, doi: [10.3847/1538-4357/ac04af](https://doi.org/10.3847/1538-4357/ac04af)
- Chung, H., Vargas, C. J., Hamden, E., et al. 2021b, in *Society of Photo-Optical Instrumentation Engineers (SPIE) Conference Series*, Vol. 11819, UV/Optical/IR Space Telescopes and Instruments: Innovative Technologies and Concepts X, ed. A. A. Barto, J. B. Breckinridge, & H. P. Stahl, 1181903, doi: [10.1117/12.2593001](https://doi.org/10.1117/12.2593001)
- Chung, H., Vargas, C. J., Hamden, E., et al. 2021c, in *Society of Photo-Optical Instrumentation Engineers (SPIE) Conference Series*, Vol. 11819, UV/Optical/IR Space Telescopes and Instruments: Innovative Technologies and Concepts X, ed. A. A. Barto, J. B. Breckinridge, & H. P. Stahl, 1181903, doi: [10.1117/12.2593001](https://doi.org/10.1117/12.2593001)
- Corlies, L., Peeples, M. S., Tumlinson, J., et al. 2020, *ApJ*, 896, 125, doi: [10.3847/1538-4357/ab9310](https://doi.org/10.3847/1538-4357/ab9310)
- Emerick, A., Bryan, G. L., & Mac Low, M.-M. 2019, *MNRAS*, 482, 1304, doi: [10.1093/mnras/sty2689](https://doi.org/10.1093/mnras/sty2689)
- Faucher-Giguère, C.-A., & Oh, S. P. 2023, *ARA&A*, 61, 131, doi: [10.1146/annurev-astro-052920-125203](https://doi.org/10.1146/annurev-astro-052920-125203)
- Grimes, J. P., Heckman, T., Strickland, D., et al. 2007, *ApJ*, 668, 891, doi: [10.1086/521353](https://doi.org/10.1086/521353)
- Ha, T., Rupke, D. S. N., Caraker, S., et al. 2025, *ApJ*, 986, 87, doi: [10.3847/1538-4357/add0b5](https://doi.org/10.3847/1538-4357/add0b5)
- Haardt, F., & Madau, P. 2012, *ApJ*, 746, 125, doi: [10.1088/0004-637X/746/2/125](https://doi.org/10.1088/0004-637X/746/2/125)
- Hayes, M., Melinder, J., Östlin, G., et al. 2016, *ApJ*, 828, 49, doi: [10.3847/0004-637X/828/1/49](https://doi.org/10.3847/0004-637X/828/1/49)
- Hummels, C. B., Smith, B. D., & Silvia, D. W. 2017, *ApJ*, 847, 59, doi: [10.3847/1538-4357/aa7e2d](https://doi.org/10.3847/1538-4357/aa7e2d)
- Hummels, C. B., Smith, B. D., Hopkins, P. F., et al. 2019, *ApJ*, 882, 156, doi: [10.3847/1538-4357/ab378f](https://doi.org/10.3847/1538-4357/ab378f)
- Hunter, J. D. 2007, *Computing in Science and Engineering*, 9, 90, doi: [10.1109/MCSE.2007.55](https://doi.org/10.1109/MCSE.2007.55)
- Kacprzak, G. G., Churchill, C. W., & Nielsen, N. M. 2012, *ApJL*, 760, L7, doi: [10.1088/2041-8205/760/1/L7](https://doi.org/10.1088/2041-8205/760/1/L7)
- Kim, J.-A., Chung, H., Vargas, C. J., & Hamden, E. 2024, *AJ*, 168, 11, doi: [10.3847/1538-3881/ad4887](https://doi.org/10.3847/1538-3881/ad4887)
- Krishnarao, D., Fox, A. J., D'Onghia, E., et al. 2022, *Nature*, 609, 915, doi: [10.1038/s41586-022-05090-5](https://doi.org/10.1038/s41586-022-05090-5)
- Kusakabe, H., Mauerhofer, V., Verhamme, A., et al. 2024, arXiv e-prints, arXiv:2406.04399, doi: [10.48550/arXiv.2406.04399](https://doi.org/10.48550/arXiv.2406.04399)
- Lan, T.-W., & Mo, H. 2018, *ApJ*, 866, 36, doi: [10.3847/1538-4357/aadc08](https://doi.org/10.3847/1538-4357/aadc08)
- Lehner, N., Howk, J. C., Tripp, T. M., et al. 2013, *ApJ*, 770, 138, doi: [10.1088/0004-637X/770/2/138](https://doi.org/10.1088/0004-637X/770/2/138)
- Lehner, N., Berek, S. C., Howk, J. C., et al. 2020, *ApJ*, 900, 9, doi: [10.3847/1538-4357/aba49c](https://doi.org/10.3847/1538-4357/aba49c)
- Lehner, N., Howk, J. C., Collins, L., et al. 2025a, arXiv e-prints, arXiv:2506.16573, doi: [10.48550/arXiv.2506.16573](https://doi.org/10.48550/arXiv.2506.16573)
- Lehner, N., Howk, J. C., Collins, L., et al. 2025b, arXiv e-prints, arXiv:2506.16573, doi: [10.48550/arXiv.2506.16573](https://doi.org/10.48550/arXiv.2506.16573)
- Lochhaas, C., Tumlinson, J., O'Shea, B. W., et al. 2021, *ApJ*, 922, 121, doi: [10.3847/1538-4357/ac2496](https://doi.org/10.3847/1538-4357/ac2496)
- Lochhaas, C., Tumlinson, J., Peeples, M. S., et al. 2023, *ApJ*, 948, 43, doi: [10.3847/1538-4357/acbb06](https://doi.org/10.3847/1538-4357/acbb06)
- Lochhaas, C., Peeples, M. S., O'Shea, B. W., et al. 2025, arXiv e-prints, arXiv:2510.25844. <https://arxiv.org/abs/2510.25844>
- Lokhorst, D., Abraham, R., van Dokkum, P., Wijers, N., & Schaye, J. 2019a, *ApJ*, 877, 4, doi: [10.3847/1538-4357/ab184e](https://doi.org/10.3847/1538-4357/ab184e)
- Lokhorst, D., Abraham, R., van Dokkum, P., Wijers, N., & Schaye, J. 2019b, *ApJ*, 877, 4, doi: [10.3847/1538-4357/ab184e](https://doi.org/10.3847/1538-4357/ab184e)
- Lopez, S., Tejos, N., Barrientos, L. F., et al. 2020, *MNRAS*, 491, 4442, doi: [10.1093/mnras/stz3183](https://doi.org/10.1093/mnras/stz3183)

- Martin, D. C., O'Sullivan, D., Matuszewski, M., et al. 2019, *Nature Astronomy*, 3, 822, doi: [10.1038/s41550-019-0791-2](https://doi.org/10.1038/s41550-019-0791-2)
- McDermid, R. M., Bacon, R., Bauer, S., et al. 2008, in 2007 ESO Instrument Calibration Workshop, ed. A. Kaufer & F. Kerber, 325, doi: [10.1007/978-3-540-76963-7_44](https://doi.org/10.1007/978-3-540-76963-7_44)
- Melso, N., Schiminovich, D., Sitaram, M., et al. 2024, *ApJ*, 974, 161, doi: [10.3847/1538-4357/ad6cd1](https://doi.org/10.3847/1538-4357/ad6cd1)
- Melso, N., Schiminovich, D., Smiley, B., et al. 2022, *ApJ*, 941, 185, doi: [10.3847/1538-4357/ac9d9c](https://doi.org/10.3847/1538-4357/ac9d9c)
- Miles, D. M., Picouet, V., Lin, Z., et al. 2025, *ApJS*, 278, 58, doi: [10.3847/1538-4365/add15c](https://doi.org/10.3847/1538-4365/add15c)
- Morrissey, P., Matuszewski, M., Martin, D. C., et al. 2018, *ApJ*, 864, 93, doi: [10.3847/1538-4357/aad597](https://doi.org/10.3847/1538-4357/aad597)
- Nielsen, N. M., Churchill, C. W., & Kacprzak, G. G. 2013, *ApJ*, 776, 115, doi: [10.1088/0004-637X/776/2/115](https://doi.org/10.1088/0004-637X/776/2/115)
- Nielsen, N. M., Fisher, D. B., Kacprzak, G. G., et al. 2024, *Nature Astronomy*, 8, 1602, doi: [10.1038/s41550-024-02365-x](https://doi.org/10.1038/s41550-024-02365-x)
- Otte, B., Murphy, E. M., Howk, J. C., et al. 2003, *ApJ*, 591, 821, doi: [10.1086/375535](https://doi.org/10.1086/375535)
- Peeples, M. S., Werk, J. K., Tumlinson, J., et al. 2014, *ApJ*, 786, 54, doi: [10.1088/0004-637X/786/1/54](https://doi.org/10.1088/0004-637X/786/1/54)
- Peeples, M. S., Corlies, L., Tumlinson, J., et al. 2019, *ApJ*, 873, 129, doi: [10.3847/1538-4357/ab0654](https://doi.org/10.3847/1538-4357/ab0654)
- Planck Collaboration, Ade, P. A. R., Aghanim, N., et al. 2016, *A&A*, 594, A13, doi: [10.1051/0004-6361/201525830](https://doi.org/10.1051/0004-6361/201525830)
- Pontzen, A., & Tremmel, M. 2018, *ApJS*, 237, 23, doi: [10.3847/1538-4365/aac832](https://doi.org/10.3847/1538-4365/aac832)
- Prochaska, J. X., Werk, J. K., Worseck, G., et al. 2017, *ApJ*, 837, 169, doi: [10.3847/1538-4357/aa6007](https://doi.org/10.3847/1538-4357/aa6007)
- Shaban, A., Bordoloi, R., O'Meara, J. M., et al. 2025, *ApJ*, 986, 190, doi: [10.3847/1538-4357/add0b9](https://doi.org/10.3847/1538-4357/add0b9)
- Simons, R. C., Peeples, M. S., Tumlinson, J., et al. 2020, *ApJ*, 905, 167, doi: [10.3847/1538-4357/abc5b8](https://doi.org/10.3847/1538-4357/abc5b8)
- Simons, R. C., Peeples, M. S., Tumlinson, J., et al. 2024, arXiv e-prints, arXiv:2409.17244, doi: [10.48550/arXiv.2409.17244](https://doi.org/10.48550/arXiv.2409.17244)
- Smith, B. D., Turk, M. J., Sigurdsson, S., O'Shea, B. W., & Norman, M. L. 2009, *ApJ*, 691, 441, doi: [10.1088/0004-637X/691/1/441](https://doi.org/10.1088/0004-637X/691/1/441)
- Smith, B. D., Bryan, G. L., Glover, S. C. O., et al. 2017, *MNRAS*, 466, 2217, doi: [10.1093/mnras/stw3291](https://doi.org/10.1093/mnras/stw3291)
- Taira, E., Koppenhafer, C., O'Shea, B. W., et al. 2025, *ApJ*, 991, 221, doi: [10.3847/1538-4357/adfc4e](https://doi.org/10.3847/1538-4357/adfc4e)
- The LUVOIR Team. 2019, arXiv e-prints, arXiv:1912.06219, doi: [10.48550/arXiv.1912.06219](https://doi.org/10.48550/arXiv.1912.06219)
- Trapp, C. W., Peeples, M. S., Tumlinson, J., et al. 2025, arXiv e-prints, arXiv:2511.00158, <https://arxiv.org/abs/2511.00158>
- Tumlinson, J., Peeples, M. S., & Werk, J. K. 2017, *ARA&A*, 55, 389, doi: [10.1146/annurev-astro-091916-055240](https://doi.org/10.1146/annurev-astro-091916-055240)
- Tumlinson, J., Thom, C., Werk, J. K., et al. 2011, *Science*, 334, 948, doi: [10.1126/science.1209840](https://doi.org/10.1126/science.1209840)
- Tumlinson, J., Thom, C., Werk, J. K., et al. 2013, *ApJ*, 777, 59, doi: [10.1088/0004-637X/777/1/59](https://doi.org/10.1088/0004-637X/777/1/59)
- Turk, M. J., Smith, B. D., Oishi, J. S., et al. 2011, *The Astrophysical Journal Supplement Series*, 192, 9, doi: [10.1088/0067-0049/192/1/9](https://doi.org/10.1088/0067-0049/192/1/9)
- van de Voort, F., Springel, V., Mandelker, N., van den Bosch, F. C., & Pakmor, R. 2019, *MNRAS*, 482, L85, doi: [10.1093/mnras/sly190](https://doi.org/10.1093/mnras/sly190)
- Virtanen, P., Gommers, R., Oliphant, T. E., et al. 2020, *Nature Methods*, 17, 261, doi: [10.1038/s41592-019-0686-2](https://doi.org/10.1038/s41592-019-0686-2)
- Vorobiev, D. 2025, in *American Astronomical Society Meeting Abstracts*, Vol. 246, 246th Meeting of the American Astronomical Society, 141.03
- Walt, S. v. d., Colbert, S. C., & Varoquaux, G. 2011, *Computing in Science & Engineering*, 13, 22
- Wendt, M., Bouché, N. F., Zabl, J., Schroetter, I., & Muzahid, S. 2021, *MNRAS*, 502, 3733, doi: [10.1093/mnras/stab049](https://doi.org/10.1093/mnras/stab049)
- Werk, J. K., Prochaska, J. X., Tumlinson, J., et al. 2014, *ApJ*, 792, 8, doi: [10.1088/0004-637X/792/1/8](https://doi.org/10.1088/0004-637X/792/1/8)
- Wisotzki, L., Bacon, R., Brinchmann, J., et al. 2018, *Nature*, 562, 229, doi: [10.1038/s41586-018-0564-6](https://doi.org/10.1038/s41586-018-0564-6)
- Witt, E. M., Fleming, B. T., McCandliss, S., et al. 2025, in *UV, X-Ray, and Gamma-Ray Space Instrumentation for Astronomy XXIV*, Vol. 13625, SPIE, 173–181
- Wright, A. C., Tumlinson, J., Peeples, M. S., et al. 2024, *ApJ*, 970, 70, doi: [10.3847/1538-4357/ad49a3](https://doi.org/10.3847/1538-4357/ad49a3)
- Zahedy, F. S., Chen, H.-W., Johnson, S. D., et al. 2019, *MNRAS*, 484, 2257, doi: [10.1093/mnras/sty3482](https://doi.org/10.1093/mnras/sty3482)
- Zheng, Y., Peeples, M. S., O'Shea, B. W., et al. 2020, *ApJ*, 896, 143, doi: [10.3847/1538-4357/ab960a](https://doi.org/10.3847/1538-4357/ab960a)